Evaluating Effects of Host Cell Membrane Inhomogeneity on Influenza Viral Interaction: A Modeling Approach

---

A Thesis

Presented to

the faculty of the School of Engineering and Applied Science

University of Virginia

---

in partial fulfillment
of the requirements for the degree

Master of Science

by

Cara J. Broshkevitch

August 2018

APPROVAL SHEET

This Thesis
is submitted in partial fulfillment of the requirements
for the degree of
Master of Science

Author Signature: _____

This Thesis has been read and approved by the examining committee:

Advisor: Dr. Peter Kasson

Committee Member: Dr. Jason Papin

Committee Member: Dr. David Green

Committee Member: _____

Committee Member: _____

Committee Member: _____

Accepted for the School of Engineering and Applied Science:

Craig H. Benson, School of Engineering and Applied Science

August 2018

Abstract

Despite influenza's continued presence as a global health threat, no treatment yet exists that provides lasting and comprehensive protection against all viral strains. The constant genetic change of influenza surface proteins prevents development of a universal vaccine, increasing the attractiveness of therapeutics that target host cells rather than the virus. It is of particular interest to identify host cell membrane features that influence viral attachment and downstream infection. In this regard, increased membrane concentration of cholesterol has been shown to increase viral binding. Subsequent molecular dynamics (MD) simulations reveal transient clustering of influenza receptors, and further stabilization of these clusters by cholesterol. These results suggest that membrane receptor and cholesterol composition influence viral attachment by modulating membrane spatial patterning and dynamics.

Here we present a novel computational approach that allows mechanistic study of the molecular behavior of host membrane components, while also capturing the relationship between large-scale membrane organization and multivalent influenza interaction. We reparametrize an existing viral binding and dynamics module for influenza, but add a new membrane module featuring receptors responsive to both thermodynamics and viral attachment. Validation analyses suggest that our Langevin dynamics membrane model displays membrane characteristics reflective of higher-resolution MD simulations. Specifically, we observe a statistically equivalent receptor cluster size distribution and receptor dissociation rate comparable or greater than MD simulations. Our approach thus maintains essential aspects of molecular-level membrane physics while increasing efficiency to allow physiological-scale study of factors influencing influenza attachment.

However, simulations of virus-membrane interaction demonstrate that our model underestimates multivalent viral binding compared to experiment. Although metrics such as mean number of bound receptors and proportion time bound tended to increase with receptor concentration, a statistically significant increase in binding was only observed between the most extreme receptor concentrations. Similarly, our simulations did not produce binding trends responsive to GD1a self-interaction with high fidelity. In conjunction with lack of sensitivity to varied cholesterol composition, these results suggest our model is not sufficiently powered to detect differences in localized receptor spatial patterning and dynamics. However, inconsistent agreement between simulated and experimental observations of influenza binding behavior provide an opportunity for us to reexamine fundamental assumptions such as the relative impact on viral binding of membrane deformation and other forces. The current model provides a well-defined framework to implement these future modifications and additions.

Acknowledgements

First and foremost, I would like to thank my advisor, Dr. Peter Kasson, for his guidance throughout my time as both a graduate and undergraduate student at the University of Virginia (UVa). His lab shaped my research experience for the latter half of my time at UVa, and my fourth year capstone project grew to be the graduate thesis presented here. As I've built my computational and statistical toolset from the ground up, I am grateful to Dr. Kasson for challenging me to think deeply about the science and choose the method because it's appropriate, not because it's easy.

I would also like to thank my committee members Dr. Jason Papin, Dr. Peter Kasson, and Dr. David Green for their input on my thesis. Their expertise improved my project and has made me a better researcher and thinker.

This work would not have been possible without the help and support of all my current and former lab mates: Dr. George Cortina, Dr. Ricardo Ferreira, Isabel Goronzy, Jennifer Hays, Dr. Eric Irrgang, Dr. Kenta Okamoto, Dr. Ania Pabis, Dr. Bob Rawle, Dr. Anjali Sengar, Dr. Ana Villamil Giraldo, and Kasia Zawada. All of these people have provided a listening ear, suggestions, and encouragement during the course of this project. I would particularly like to thank Jennifer Hays and Dr. Eric Irrgang for their technical help with various computational methods- they are both excellent teachers. Lastly, I want to acknowledge the staff both at Fontaine and in the Biomedical Engineering department that support us daily.

Special thanks go to the numerous Biomedical Engineering faculty who have been mentors for me along this journey. I would especially like to highlight Dr. Jason Papin, as well as Dr. Timothy Allen, Dr. Shayn Peirce-Cottler, and Dr. Song Hu. These professors encouraged me to pursue a Master's degree, and provided support both inside and outside the classroom.

Finally, I would like to thank my fiancé Christopher Bayer, as well as my parents Mark and Andrea, for their tireless encouragement. Their guidance and support were pivotal to completion of this thesis.

Table of Contents

Table of Figures and Tables

Chapter 1. Introduction

1.1 Influenza: A global health threat with limited clinical solutions

Influenza is a deadly and communicable virus that causes 12,000 to 56,000 deaths annually in the United States, with the yearly number fluctuating due to variability and unpredictability of the flu season (1). The virus presents a global public health problem as transmission can occur through non-human hosts, accelerating antigenic shift and development of new, possibly pandemic strains. Despite this risk, no universal vaccine exists that provides lasting protection against multiple influenza strains. The constant genetic change of influenza surface proteins impedes the effective antibody targeting, binding, and neutralization required of such a solution. Antiviral therapeutics therefore play an essential role in supporting the functionally-limited seasonal vaccine.

However, the two classes of influenza antiviral drugs currently approved by the United States Food and Drug Administration (FDA) face increasing evidence of viral resistance (2–5). These drugs, adamantanes and neuraminidase inhibitors, target the viral proteins necessary for viral budding, preventing escape and infection of additional cells (6). Recently, a novel class of influenza therapeutics that target host cell machinery rather than viral components began early-stage development, offering decreased risk of emergent resistant strains (7). Advancement of host-targeted therapeutics remains limited by a lack of understanding of the host factors that influence viral attachment and subsequent steps in the infection process.

1.2 Influenza binding is multivalent

Influenza infection begins when the viral hemagglutinin (HA) glycoprotein binds to sialic acid (SA)-terminated glycans (sialosaccharides) in the host cell membrane (**Figure 1**) (8). Stable binding then leads to endocytosis of the virus. Gradual acidification of the encapsulating endosome triggers fusion of the viral envelope with the endosomal membrane. Fusion allows release of viral RNA into the host cell cytoplasm, and downstream replication of the virus.

Much attention has been given to understanding how host membrane glycan structure affects the affinity of individual HA glycoproteins across influenza strains. Of particular interest, is the linkage between a sialic acid and the penultimate galactose residues of sialosaccharides (8). The α(2,3) linkage is associated with avian influenza strains and leads to enteric infection, while the α(2,6) linkage is

associated with human influenza strains and results in the familiar respiratory illness. A shift in HA genetics to allow specific binding to the α(2,6)-type linkage is often accompanied by increased viral transmissibility between humans (9–11).

However, the dissociation constant for an individual HA to either sialic acid linkage remains ubiquitously low (mM range) (12). This low HA-sialic acid affinity suggests that influenza binding is multivalent, or that multiple HA-SA attachments are necessary for stable binding. Multivalent binding is supported by cryo-electron tomography experiments that demonstrate influenza-membrane binding areas of 100 to 600 nm^2, with the target membrane parallel to the viral envelope for up to 100 nm (13,14).

Evidence that influenza binds multivalently to host cell receptors raises a question of the relative importance of equilibrium spatial patterning of host receptors compared to time-dependent, large-scale remodeling of receptor patterning by viral interaction. It has been shown that the force of membrane attachment to the viral envelope increases with time, suggesting that mobile receptors may be recruited beneath the influenza virus (15). Single-virus tracking studies corroborate that host membrane remodeling fits within the time-course of influenza infection. These experiments detect clatherin-coated pit formation approximately 115 seconds after initial viral binding (16). With multiple receptor binding and dissociation events thought possible on the order of seconds, this timescale allows for receptor movement before clatherin-mediated endocytosis of the virus. However, the dynamics and driving factors of large-scale receptor patterning and remodeling in the host cell membrane remain unexplored.

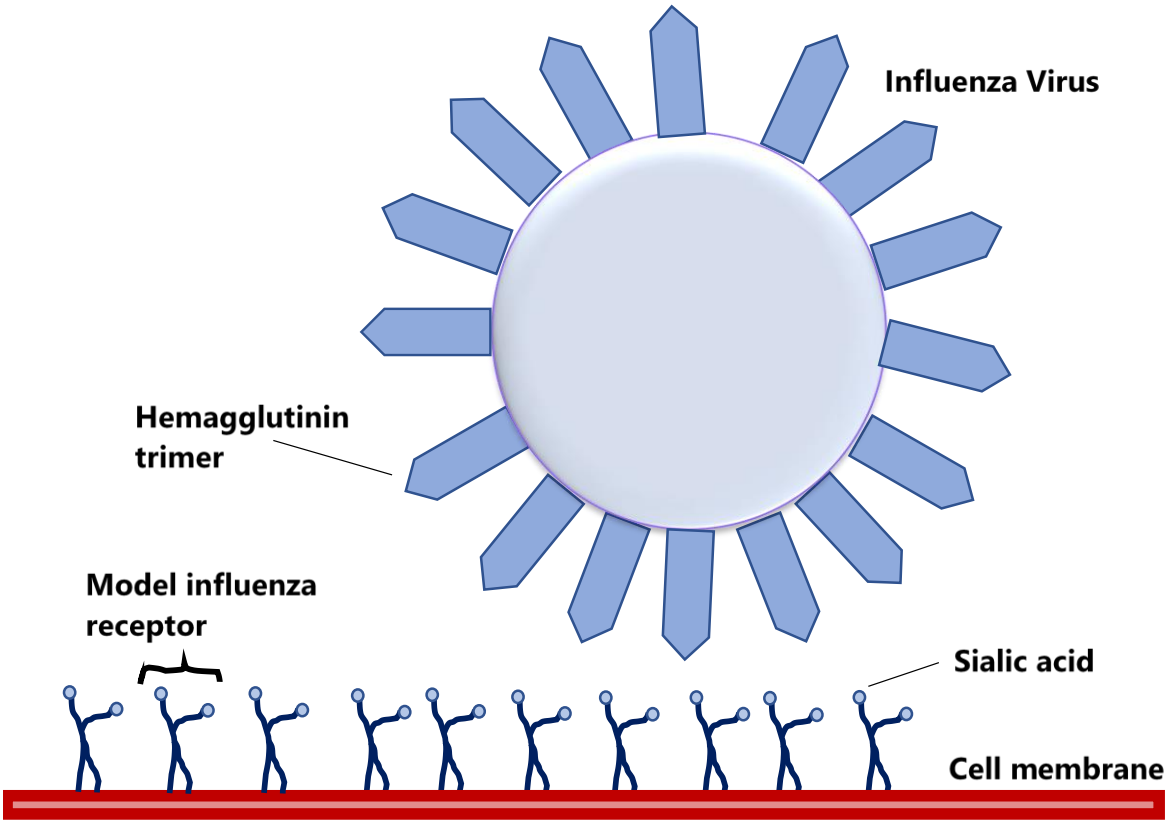

Figure 1. Sketch of influenza virus binding to a host cell membrane. Viral hemagglutinin glycoprotein binds sialic acids in the host cell membrane. Binding triggers endocytosis of the virus and transmission of viral RNA to infect the host. The model influenza receptor, GD1a, includes two sialic acids in its oligosaccharide headgroup. (Not to scale).

1.3 Cell membrane patterning and dynamics are linked to composition

The heterogeneous distribution of lipids and proteins in human plasma membrane has elicited extensive study of factors affecting the patterning of these components. Of interest are model systems combining cholesterol, phospholipids, and sphingolipids because a large body of previous work uses this simplified composition to represent human cell membrane behavior (17). Of these studies, many focus on the effect of cholesterol content on sterol-dependent "rafting" phase behavior, or the ordered clustering of specific lipid types surrounded by disordered lipids (17,18). No evidence exists of significant cholesterol-driven phase separation in membranes with a physiological concentration of glycosphingolipids (<5 mol%), the category of sphingolipid that includes the influenza receptor. However, it is known that glycosphingolipids self-associate independent of cholesterol (19).

To enable molecular-level analysis of membrane spatial patterning and dynamics, we recently developed a molecular dynamics (MD) coarse-grained (CG) membrane model using the GROMACS simulation package. MD simulations are an ideal source for dynamic data on influenza receptor patterning because they overcome fluorescence microscopy's inability to resolve nanoscale cluster sizes, a practical limitation of microscopic binding, fluidity, and detergent-resistance studies (20). Our generated MD simulations are consistent with ganglioside self-association behavior described previously, but include the influenza virus GD1a receptor (19). Ganglioside GD1a is commonly used as the model influenza receptor, including two sialic acids on its glycosphingolipid backbone (21,22). These simulations demonstrate that increased cholesterol content increases receptor tail order and decreases the dissociation rate of individual GD1a glycosphingolipids from clusters (23). It is therefore thought that an increase in influenza viral binding to membranes of increased cholesterol content is due to the stabilization of transient clusters of receptors (23).

These results suggest that small-scale membrane patterning and cluster formation influence influenza viral binding. However, the molecular detail of MD simulations prohibits efficient scaling to lengths involved in viral interaction at a simulation timescale of tens of μs to minutes. For example, previous MD membrane studies include a 2-10 mol% concentration of influenza receptors over a 15 by 15 nm leaflet. All 7 to 36 of these receptors may be present in a single cluster. Therefore, an influenza virus of 105 nm diameter may interact with multiple clusters or a broader organization of receptors than can be captured by MD simulations (24). Clearly, a new method is needed that allows mechanistic study of the molecular behavior of host membrane components, while also capturing the relationship between large-scale membrane organization and multivalent influenza interaction.

1.4 Approaches to studying viral binding

Similar to the motivation for MD modeling of small-scale membrane patterning, a computational approach will allow mechanistic study of virus-scale membrane patterning and influenza attachment within nm resolution. This will allow us to extend earlier work that focuses solely on observables specific to the influenza virus (15,25). Previous work has modeled the multivalent adhesion of influenza HA to SAs, but does not account for the position-dependent variability in HA-SA affinity across the viral binding interface (26). Computational models better equipped to capture this relationship have been developed to study virus-membrane interaction, first of human immunodeficiency virus (HIV), and then of DNA tumor-causing Simian virus (SV40) (27–30). However, all present models assume fixed receptor positions or a homogeneous diffusion rate insensitive to varied membrane composition or an inhomogeneous patterning of components.

This recent work can be reparametrized to capture known information about influenza structure and diffusion, GD1a receptor structure, and rates and degrees of freedom of influenza binding and unbinding (29). We therefore have a ready framework for capturing the movement of influenza in the vicinity of the host cell membrane, as well as the interaction of the virus with the membrane through multiple HA-SA bonds across the attachment interface. This model is equipped to measure differences in binding probabilities in accordance with receptor position, but new capability to designate receptor spatial pattering responsive to both membrane thermodynamics and viral attachment is still needed. This extended model must maintain the receptor-level physics of molecular dynamics simulations, while adequately reducing resolution to achieve efficient characterization of influenza virus attachment and interaction with the host cell membrane.

1.5 This Thesis

This thesis explores the hypothesis that membrane composition affects viral binding by driving the spatial patterning of influenza receptors in the cell membrane. An extended model of influenza binding to a human cell is described. First, we attempt to validate a reduced-resolution, Langevin dynamics model of membrane patterning and movement derived from molecular dynamics membrane simulation data. Second, an approach is presented for linking inhomogeneous membrane patterning and dynamics to mesoscopic viral motion and interaction forces. This model predicts viral binding outcomes correlated but not completely consistent with those observed from experimental changes in membrane composition. The framework is then used to mechanistically explore the effect of membrane

composition and localized receptor patterning on viral binding. Finally, we evaluate the relative importance of the equilibrium patterning of receptors in an individual's cell membrane compared to active remodeling of that membrane pattern over time by viral interaction. This computational approach, with the later-described improvements, offers the potential for an improved understanding of membrane factors influencing an individual's susceptibility to influenza infection. Several viruses including influenza, mumps, noro, rota, and DNA tumor viruses bind to the same group of sialic acids linked to gangliosides or glycoproteins as a receptor during cell entry. Our influenza-focused methodology may therefore be extended as a tool to reveal novel targets for development of lipid-based antiviral therapies to reduce viral infection.

Chapter 2. Model Development

2.1 Chapter Introduction

The proposed modeling approach can be schematized as two modules, a mesoscopic viral dynamics and binding module adapted from previous work, and a newly parameterized membrane dynamics module. These two components exchange the identities and relative position coordinates of bound HA-SA pairs to determine the forces that drive influenza-membrane interaction. We first describe the mesoscopic viral dynamics and binding module, followed by the development and validation of the membrane dynamics module.

2.2 Methods

2.2.1 Parameterization of a mesoscopic binding model for influenza

2.2.1.1 Viral structure

Using open source code made available in the literature, we reparametrized the mesoscopic viral dynamics and binding module to accurately capture influenza structure and behavior (29). We modeled influenza as spherical with a diameter of 104.862 nm, including the height of 300 protruding 13.5 nm hemagglutinin spikes (24,31). The current parameterization assumes that hemagglutinin can be approximated as immobile and evenly distributed throughout the viral envelope (32). Hemagglutinin is known to exist as a homotrimer and concurrent binding of three sialic acids to single binding sites on each polypeptide is thought to be geometrically possible (25). Therefore, each viral hemagglutinin was represented as a single point on the viral envelope, and incorporates three binding points.

2.2.1.2 Viral dynamics algorithm

In each simulation, a virus was generated in a rectangular box near to the membrane and began a 3D random walk until contacting the cell surface (**Figure 2a**). The viral space was divided into “near” and “far” regimes based on the likelihood of viral binding and unbinding events as previously described in literature and detailed in **Figure 2b** (27–30). The virus moved randomly in the far regime, diffusing according to the Stokes-Einstein equation with an adaptive, distance-dependent time step (29). In the near regime, the virus moved both translationally according to a velocity Verlet stochastic dynamics

algorithm and rotationally according to a quaternion dynamics algorithm, at a fixed time step of 1.5 ns (29).

This regional division and an initial start point near to the membrane allowed increased sampling of viral behavior near to the membrane for parameterizations where binding is rare and multiple virus-membrane interaction events were needed before the virus binds stably. These assumptions were appropriate for the present study in which we aimed to assess the physics of viral interaction and receptor spatial remodeling rather than how these events fit into the broader timescale of influenza infection.

Virus movement was modeled using Langevin dynamics. Near to the membrane, the virus was subject to both stochastic forces from random thermal motion of the virus and deterministic forces due to receptor binding. The position and velocity of the virus were described by differential **Equations 1-3**:

$$\frac{d\vec{r}}{dt} = \vec{v} \qquad \textit{Equation 1}$$

$$\frac{d\vec{v}}{dt} = \vec{K}(\vec{r}, t) + \ -\beta_v \vec{v} + \vec{A} \qquad \textit{Equation 2}$$

$$\beta_v = \frac{kBT}{m_v D_v} \qquad \textit{Equation 3}$$

where $\vec{r}$ is a vector of positions, $\vec{v}$ is a vector of velocities, $\vec{K}$ is a vector of accelerations due to deterministic binding forces, β_v is the inverse of the viscous relaxation time, and $\vec{A}$ is a vector of accelerations due to stochastic forces (29,30). **Equation 3** represents the inverse of the viscous relaxation time β_v as a function of Boltzmann constant kB, temperature T, mass of the virus m_v, and diffusion coefficient of the virus D_v (29,30). In another form multiplied by mass, β_v represents a drag coefficient. Stochastic forces captured the random collision of the virus with implicit solvent particles.

Deterministic HA-receptor attachment forces were governed by a harmonic bond potential according to **Equation 4**:

$$V(r) = \frac{1}{2}\sigma(r - r_0) \qquad \textit{Equation 4}$$

In this equation, σ represents the spring force constant of the bond, r represents the vector between the viral hemagglutinin and GD1a receptor, and r_0 represents the equilibrium, unstressed height of the GD1a receptor headgroup above the membrane surface (29). Therefore, movement of the virus toward the membrane surface reduced viral forces due to any HA-SA bonds, and movement away increased forces as HA-SA bonds were stretched. r_0 was approximated as 2 nm by measuring the distance on a GD1a between the partial density peaks of one of the furthest-branched beads on the terminal SA

(GM22 bead) and the intersection between the GD1a headgroup and lipid tail (AM1 bead). The spring constant σ was derived from optical tweezers force spectroscopy force per distance curves prior to bond rupture (25).

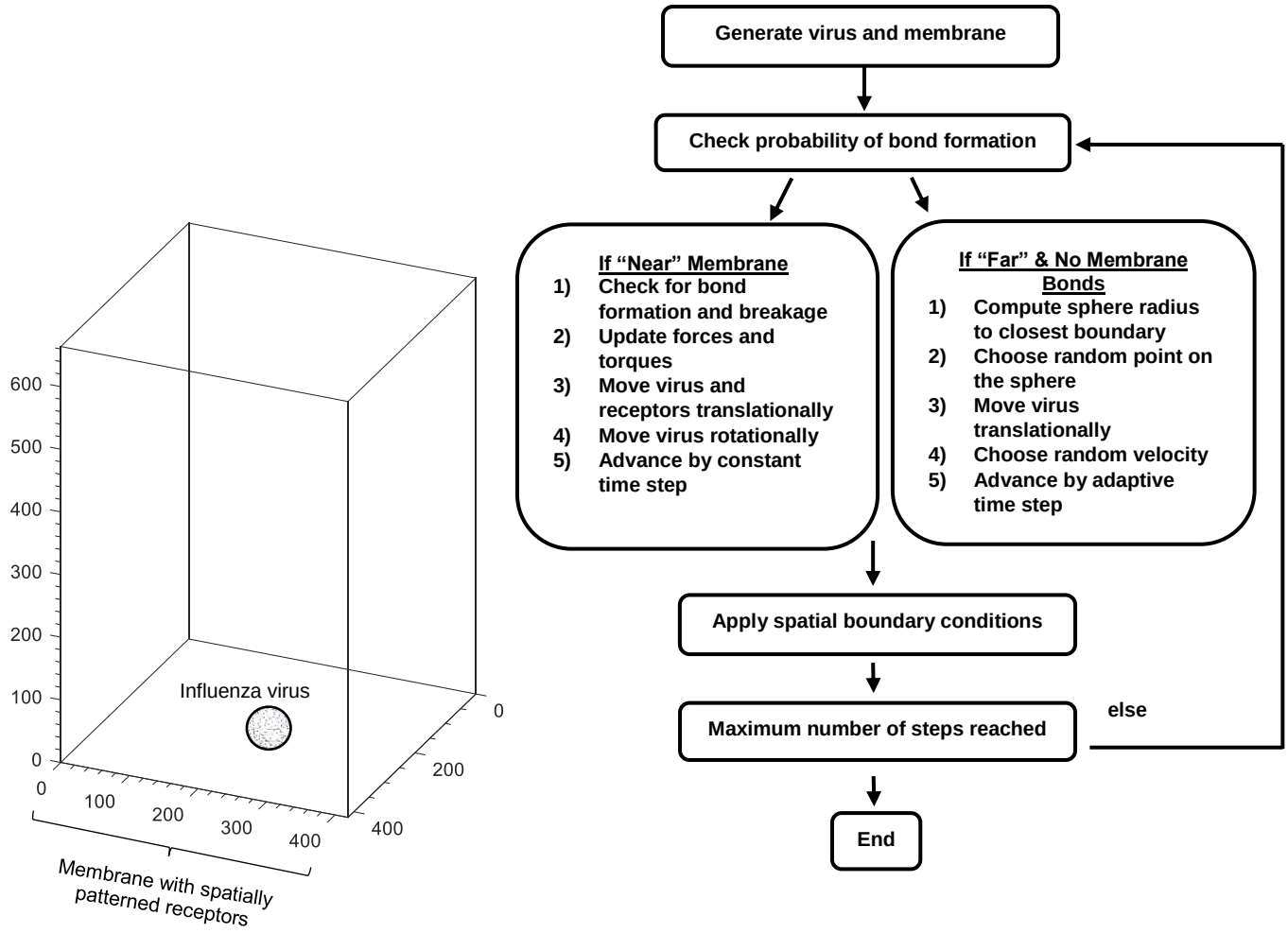

Figure 2. Framework for mesoscopic viral binding and dynamics module. (a) Graphical representation of the mesoscopic module. A single virus moves three-dimensionally and engages with a planar membrane spatially patterned with receptors. **(b)** Flowchart describing the algorithm behind the mesoscopic portion of the model reparametrized from previous work.

2.2.1.3 Viral binding algorithm

In order to capture the effect of receptor spatial patterning on viral binding, it was important to analyze individual binding events. Formation and breakage of bonds was modeled as a stochastic process, and a previously developed kinetic Monte Carlo scheme was used to evaluate the state of individual bonds at each time step (27–30). For each HA-receptor pair, the rate of bond formation k_f or breakage k_b was sampled from the probability distribution given in **Equation 5** or **6**:

$$k_f = k_f^0 \, exp\left(-\frac{\sigma_{ts}(r-r0)^2}{2\ kB\ T}\right) \qquad \textbf{\textit{Equation 5}}$$

$$k_b = k_b^0 \, exp\left(-\frac{(\sigma-\sigma_{ts})(r-r0)^2}{2\ kB\ T}\right) \qquad \textbf{\textit{Equation 6}}$$

Rates depended on the intrinsic rate constants of bond formation k_f^0 or breakage k_b^0, the bond spring constant σ, the transition state bond spring constant σ_{ts}, the equilibrium unstressed bond height r_0, and the system temperature *T*. It was assumed that set ratios between rate constants and spring constants, as well as order of magnitude approximations, could provide adequate parameterization for influenza binding behavior. Therefore, σ_{ts} was asigned as less than σ in order to meet transition state criteria for a non-catch-bond (33). The ratio between rate constants was determined using **Equation 7** (29):

$$\frac{k_b^0}{k_f^0} = K_D\left(\frac{4}{3}{R_{AB}}^3\right) \qquad \textbf{\textit{Equation 7}}$$

The dissociation constant K_D was defined as 11.4 mM for influenza strain X-31 (226 Leu) binding to GD1a (12). R_{AB} describes the radius of a sphere around a GD1a binding point, within which the GD1a can directly interact with an influenza HA, and was set to 0.75 nm as previously used in viral binding models (28,29,34). k_b^0 was set by a previous parameter screen, and used to calculate k_f^0. Rate values aligned with similar estimated values (15).

Rates of bond formation or breakage were then used to calculate the probability of bond formation $P_f(\delta t_v)$ or breakage $P_b(\delta t_v)$ at each time step δt_v as given in **Equation 8** or **9**:

$$P_f(\delta t_v) = 1 - exp(-k_f\, \delta t_v) \qquad \textbf{\textit{Equation 8}}$$

$$P_b(\delta t_v) = 1 - exp(-k_b\, \delta t_v) \qquad \textbf{\textit{Equation 9}}$$

Finally, this probability of bond formation or breakage was compared to a uniformly distributed random number. If the random number was lower than the probability of bond formation or breakage, the bond was formed or broken, respectively. To increase efficiency, only geometrically viable bonds were evaluated for formation or breakage at each time step. Receptors were only checked for formation within a cut-off radius of two-times viral diameter, and only HA proteins on the lower hemisphere of the virus were evaluated (29).

HA-receptor bonds were expected to be more flexible in the vertical direction than the lateral direction, primarily due to vertical deformability of the host cell membrane. To increase model agreement with influenza-specific multivalent binding behavior, the harmonic spring potential was modified to differentially adjust binding probability along different axes. Instead of only including HA-receptor molecular forces in this potential, additional membrane forces were combined together into an empirical model of virus-membrane interaction. This allowed the model to more accurately capture the virus-membrane interaction forces that would affect large-scale membrane remodeling. Bond flexibility along the vertical axis was expected to be a function of hemagglutinin and receptor stretch, as well as the general deformability of the membrane. Variation in GD1a headgroup height was thought to be minimal, and was accounted for by r_0 (35). Negligible energy penalty was expected with compression of the GD1a headgroup, so a flat-bottomed potential was used within r_0 of the membrane. Similarly, hemagglutinin has been shown to be rigid and this fixed length is incorporated in the viral diameter (25). Optical tweezers experiments measure cell membrane deformation up to 133 nm before bond rupture with high bond specificity (25). Therefore, membrane deformation accounts for the majority of z-axis bond flexibility, and bond formation is considered up to a maximum distance of 187.431 nm from the membrane ($r_0 + \frac{d_v}{2} + d_{FAR}$). If the virus has moved outside this range and no bonds are present, the virus follows the "far" algorithm for efficiency because probability of bond formation is low. In our model, the reference membrane is thus considered to be planar, and membrane deformation is modeled implicitly within the model of bond formation and breakage. By comparison, little lateral bond flexibility is expected beyond tilt of the GD1a receptor. Therefore, probabilities of bond formation and breakage were smoothed to zero or one, respectively, if the HA-receptor lateral distance was greater than 2 nm, the maximum GD1a headgroup length.

Table 1. Parameters for mesoscopic viral binding and dynamics module.

Parameter	Symbol	Value	Source
Virus diameter	d_v	104.8620 nm (including 13.5 nm hemagglutinin spike length)	(24)
Virus mass	m_v	0.80 fg	(36)
Virus diffusion coefficient	D_v	0.00626455 nm^2/ns	Stokes-Einstein Equation with influenza diameter including HA spike length
Number viral hemagglutinin	n_h	300	(31)
GD1a headgroup equilibrium unstressed height above membrane surface	r_0	2.0 nm	MD simulations and (35)
Bond spring constant	σ	2.672 x 10^{-4} N/m	(25)
Encounter complex bond spring constant	σ_{ec}	1.336 x 10^{-4} N/m	(33)
Standard intrinsic rate of bond breakage	k_b^0	10^{-5} ns^{-1}	UVA BME Capstone parameter screen and (15)
Standard intrinsic rate of bond formation	k_f^0	k_b^0 x 82.457 ns^{-1}	(15,28,29,34)
Fixed simulation time step in the near regime	δt_v	1.5 ns	Time step chosen to be greater than the harmonic bond frequency of a HA-receptor bond and less than the expected time for a virus to multivalently detach and reattach
Temperature	T	310 K	Temperature used in MD simulations
Maximum vertical membrane deformation	d_{FAR}	133 nm	(25)

2.2.2 Design and parameterization of a simplified membrane model

In addition to the mesoscopic virus module, a new membrane module was needed to study the effect of composition-driven inhomogeneous receptor patterning on the dynamics and outcome of multivalent influenza-membrane interactions. This module needed to accurately compute receptor coordinates based on both thermodynamic lipid behavior and changes to that behavior by viral interaction forces. We developed a membrane model that uses Langevin dynamics to capture the movement of influenza receptors, represented as single particles within a plane of implicit lipid components. Validation analyses demonstrated that this membrane model maintains the receptor-level physics of molecular dynamics simulations, while adequately reducing resolution to achieve efficient characterization of influenza virus attachment and interaction with the host cell membrane.

2.2.2.1 Membrane structure

Wall-clock and resource efficiency of the membrane model was significantly increased compared to MD simulations by reducing the resolution of membrane components. For the same membrane size, our simplified Langevin dynamics model could run in a matter of days a simulation that would require weeks with a MD membrane model. Influenza GD1a receptors were rendered as single particles with one binding point rather than three-dimensional structures of three-atom beads as used in previous coarse-grained MD simulations. Other lipid components and the surrounding solution were modeled implicitly. Representation of GD1a as a single particle was supported by evidence that the virus binds preferably to a SA in the terminal position (37). The ability of two sialic acids on a single GD1a to bind two binding sites on a single HA is also disputed (15). It was therefore assumed that this simplified receptor representation was adequate for capturing large-scale membrane patterning, and that detailed structural information on individual virus-receptor interactions was not needed.

Efficiency gained by this simplified membrane representation allowed membrane size to be increased to 419.4 by 419.4 nm in the xy-plane, compared to the 15 by 15 nm lateral box size used in previous MD simulations. This scaling achieved a two-dimensional edge length equal to four-times viral diameter. It was important that the membrane was larger than the viral cross-sectional area to avoid artifacts caused by a high probability of viral access and attachment to the whole membrane surface.

2.2.2.2 Membrane dynamics algorithm

Our streamlined membrane model captured receptor membrane dynamics by integrating GD1a behavior forward in time according to Langevin **Equations 10-14**:

$$\frac{d\vec{r}}{dt} = \vec{v} \qquad \textit{Equation 10}$$

$$\frac{d\vec{v}}{dt} = \vec{K}(\vec{r}, t) + -\beta_r \vec{v} + \vec{A} \qquad \textit{Equation 11}$$

$$\beta_r = \frac{kBT}{m_r D_r} \qquad \textit{Equation 12}$$

$$\langle \vec{A} \rangle = 0 \qquad \textit{Equation 13}$$

$$\langle \left| \vec{A} \right|^2 \rangle = \frac{2\ d\ kBT\ \beta_r\ m_r}{\delta t} \qquad \textit{Equation 14}$$

where $\vec{r}$ is a vector of positions, $\vec{v}$ is a vector of velocities, $\vec{K}$ is a vector of accelerations due to deterministic binding forces, β_r is the inverse of the viscous relaxation time, and $\vec{A}$ is a vector of accelerations due to stochastic forces. $\vec{K}$ included receptor acceleration due to all potentials and constraint forces. **Equation 12** represents the inverse of the viscous relaxation time β_r as a function of the Boltzmann constant kB, temperature T, mass of the receptor m_v, and the diffusion coefficient of the receptor D_r. D_r was approximated from fluorescence recovery after photobleaching (FRAP) bulk fluidity measurements of lipid-tailed dye in a planar bilayer of similar composition. The magnitude of the random force $\overrightarrow{F_R}$ behind the stochastic acceleration $\vec{A}$ followed the fluctuation-dissipation theorem and centered around **Equations 13** and **14** where d is the dimensionality of the system.

When the virus attached to the cell membrane, the positions of viral hemagglutinin proteins were projected on to the lateral membrane plane. Net lateral forces from the HA-receptor harmonic bonds were incorporated into the $\vec{K}$ term of **Equation 11**. As in the mesoscopic viral module, HA-receptor attachment forces were governed by **Equation 4**.

HOOMD is a high performance, particle dynamics toolkit that is ideally suited for quickly running simulations constrained by parameters such as those governing influenza receptor behavior (38,39). This toolkit could be run on the GPU, compensating for a small timestep and large membrane size. Due to the significantly larger mass of the influenza virus compared to the GD1a receptors, the virus diffuses relatively slowly. Therefore, the membrane model could be run iteratively to update membrane spatial patterning at a small time-step within the larger 1.5 ns time-steps of the mesoscale

module. The assumptions underlying Langevin dynamics required the system to be underdamped, with $\frac{m_r}{\beta_r} \gg \delta t_r$. This criterion necessitated a 1 fs timestep in the membrane model.

2.2.2.3 Determining a pair potential representation of receptor interaction forces

An important element in simplification of the membrane model from molecular to Langevin dynamics was capturing GD1a-GD1a interaction as a pair potential. A pair potential describes the potential energy of a GD1a pair as a function of the distance between the two receptors, and can be used to derive interaction forces. We used MD simulations to parameterize this pair potential, and incorporated the resulting forces into the $\vec{K}$ term of **Equation 11**.

The potential of mean force (PMF) describes the free energy surface with separation distance, and provides a first-iteration approximation of the pair potential. To compute the PMF, we first measured the probability of finding a GD1a receptor a distance r from another GD1a in MD simulations. Distances were measured between GM6 headgroup backbone beads of MD GD1a receptors and sorted into bins at an interval of 0.01 nm. This analysis provided a radial distribution function (RDF). To remove discrete bin size artifacts, we applied a five-point Gaussian smoothing window, representing a Van der Waals radius of 0.26 nm. We then used the Boltzmann inversion method to quantify the GD1a PMF from this RDF (**Figure 3a**). If the PMF approximation yielded infinite potential values at low GD1a-GD1a pair distances, the maximum value was set to 55 kJ/mol, and a spline interpolation function used to smooth the potential to the highest calculated finite value. GD1a pairs were not expected to reach these close distances due to high repulsive forces.

In order to best capture the nuances of the measured GD1a pair potential, a tabulated potential was used. Pair potential and force values were provided at approximately 0.10145 nm intervals and used to interpolate all other points. To reduce the number of pair evaluations in simulations with a high number of receptors, the pair potential and force were also set to zero past a cutoff distance r_{cut} of approximately 6 nm. The entire potential was then shifted and smoothed to zero beginning at an r_{on} of 5 nm using **Equation 15** (**Figure 3b**).

$$S(r) = 1 \ for \ (r < r_{on}) \qquad \textbf{Equation 15}$$

$$S(r) = \frac{\left(r_{cut}^2 - r^2\right)^2 \left(r_{cut}^2 + 2r^2 - 3r_{on}^2\right)}{\left(r_{cut}^2 - r_{on}^2\right)^3} \ for \ (r_{on} \le r \le r_{cut})$$

$$S(r) = 0 \ for \ (r > r_{cut})$$

This process was repeated over membranes compositions with 2, 4, and 10 mol% GD1a and 0, 10, and 20 mol% cholesterol (**Figure 4b-d)**. These compositions paralleled those used in previous experimental and MD studies, and featured low mol% GD1a consistent with assumed physiological concentration (40,41). Pair potential curves derived from MD membranes with 4 mol% and 10 mol% GD1a showed increased attractive well depth with increased cholesterol composition as expected from previous dissociation rate analyses (**Figure 4c,d**) (23). Pair potential curves derived from the MD 4 mol% GD1a compositions captured distinct differences between cholesterol compositions and were used to parameterize all simulation compositions. This was justified as we expected the same dissociation rate trends to apply to both lower and higher mol% GD1a compositions. Previous MD analyses indicated decreased dissociation rate with increased cholesterol for membranes with 2 mol% GD1a, but these differences were not powered for statistical significance (23). Therefore, parameterization of 2 mol% GD1a compositions with pair potentials from membranes of increased GD1a and varied cholesterol content benefited from increased sampling. As experiments demonstrate saturation of binding at 4 mol% GD1a, pair potentials derived from 4 mol% GD1a membranes of varied cholesterol composition were also expected to better capture the underlying behavior of 10 mol% compositions. At high mol% GD1a, differences in viral binding due to varied cholesterol content may be obscured by a high degree of binding regardless of composition.

Control simulations were parameterized with a standard Lennard-Jones 6-12 potential with sigma = 0.7129 and epsilon = 0.8775 (**Figure 4a**). The potential was shifted to zero after a cutoff pair evaluation distance of 1.75 nm. This cutoff distance was chosen to be greater than 2*sigma. This LJ potential included a repulsive component to prevent particle overlap and a small attractive component, but lacked the attractive well depth reflective of GD1a clustering behavior.

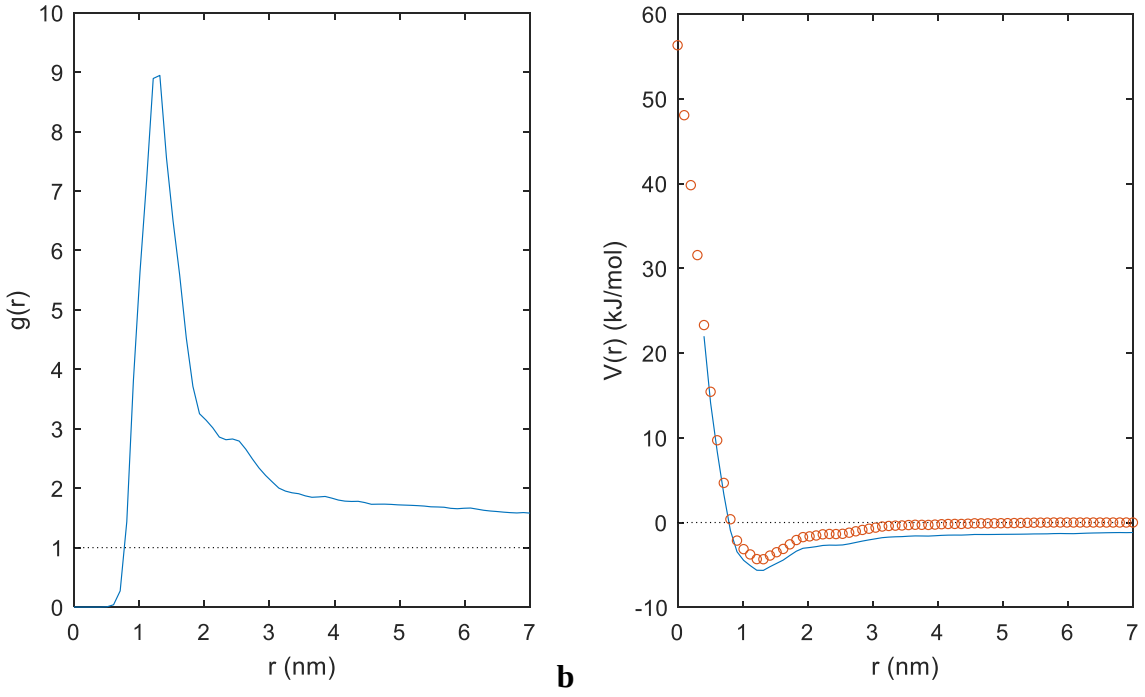

a **b**

Figure 3. Calculation of a GD1a-GD1a pair potential from the radial distribution function. (a) Gaussian-smoothed radial distribution function of the probability of finding a GD1a receptor a distance r from another GD1a in a 4 mol% GD1a, 10 mol% cholesterol molecular dynamics membrane. **(b)** GD1a-GD1a pair potential estimated from applying the Boltzmann inversion method to the radial distribution function (blue). Red circles represent the smoothed and shifted tabulated potential values used in Langevin dynamics simulations.

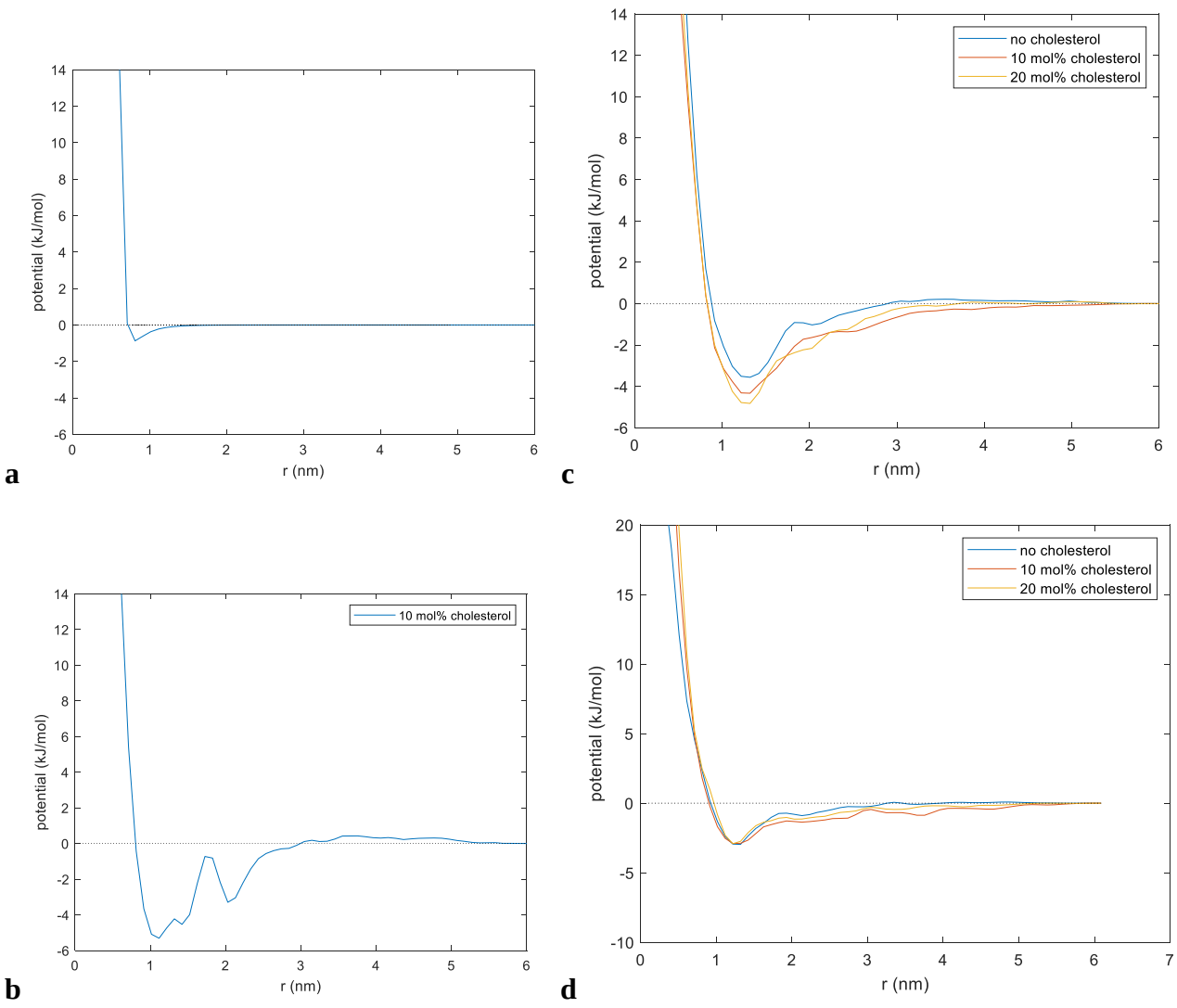

Figure 4. GD1a-GD1a pair potential varies with membrane composition. (a) Lennard-Jones 6-12 pair potential used for control simulations. **(b)** Tabulated GD1a-GD1a pair potential derived from a 2 mol% GD1a, 10 mol% cholesterol membrane. **(c)** Tabulated pair potentials derived from 4 mol% GD1a membranes of 0, 10, and 20 mol% cholesterol composition. **(d)** Tabulated pair potentials derived from 10 mol% GD1a membranes of 0, 10, and 20 mol% cholesterol composition.

Table 2. Parameters for membrane module.

Parameter	**Symbol**	**Value**
GD1a mass	m_r	0.001865 Mamu
GD1a particle diameter	d_r	1.3 nm
GD1a diffusion coefficient	D_r	2 um^2/s
Membrane edge length	L	419.4 nm
Dimensionality of the membrane	d	2
Timestep	δt_r	1 fs

2.2.3 Validation analyses

To validate that our Langevin dynamics membrane module was simple but sufficiently accurate, we compared characteristics of our membrane to those of previous MD simulations. We focused on cluster size distribution and receptor dissociation rate as two metrics that capture the core behavior of GD1a interaction and dynamics.

2.2.3.1 Cluster size distribution analysis

We quantified the size distribution of clusters across all frames of an MD membrane composed of 4 mol% GD1a, 10 mol% cholesterol, 20 mol% DOPE, and 66 mol% POPC. This membrane composition was chosen for validation analysis because pair potentials derived from MD 4 mol% GD1a membrane compositions were used to parameterize all production runs. Minimum distances between any headgroup beads were calculated across all GD1a pairs at 0.0025 μs intervals after discarding a 2.5 μs equilibration interval. Cluster contacts were defined using a distance cutoff of 0.8 nm between GD1a receptors. This corresponded to the first solvation shell. A 4 mol% GD1a MD membrane included 14 receptors per leaflet. Therefore the number of particles in clusters of size 1-14 and the evolution of this cluster membership was evaluated over all timepoints. Data from the two bilayer leaflets was averaged.

For comparison, equal length (17.46 us) Langevin dynamics simulations were analyzed at 0.0025 μs intervals, again discarding a 2.5 μs equilibration interval. Cluster contacts were defined using a distance cutoff of 1.8 nm between GD1a particles. This corresponded to the maximum spread of a GD1a headgroup. The number of particles in clusters of size 1-14 and the evolution of this cluster membership was again evaluated over all timepoints. Data from three trials was averaged.

2.2.3.2 Dissociation rate analysis

We measured the dissociation rate of a single GD1a receptor from a cluster of any size across all frames of an MD membrane composed of 4 mol% GD1a, 10 mol% cholesterol, 20 mol% DOPE, and 66 mol% POPC. Minimum distances between any headgroup beads were calculated across all GD1 pairs at 0.02 μs intervals after discarding a 2.5 μs equilibration interval. Cluster contacts were defined using a distance cutoff of 0.8 nm between GD1a receptors. To avoid artifacts caused by a hard cut-off, contacts were smoothed using a five-point moving average. A previously developed Bayesian formulation based on a Poisson event model was used to estimate dissociation rate (42). Data from the two bilayer leaflets was averaged.

For comparison, equal length Langevin dynamics simulations were analyzed at 0.02 μs intervals, again discarding a 2.5 μs equilibration interval. Cluster contacts were defined using a distance cutoff of 1.8 nm between GD1a particles. Dissociation rate was estimated as for MD simulations. Data from three trials was averaged.

2.3 Results

2.3.1 Validation of membrane cluster size distribution

If our Langevin dynamics membrane representation was simple but sufficiently accurate, membrane characteristics were expected to resemble those of molecular dynamics simulations. We evaluated the size distribution of receptor clusters and the dissociation rate of receptors from clusters as two metrics that capture receptor patterning and dynamics.

The distribution of receptor cluster sizes sampled by our Langevin dynamics membrane model was found to be in high agreement with that sampled by MD simulations of comparable length (**Figure 5**). A two-sample, two-sided Kolmogorov-Smirnov (KS) test found no statistically significant difference between Langevin and MD distributions of particles in clusters of size 1-14 ($\alpha = 0.05$). However, it should be noted that Langevin clusters were slightly more stable than MD clusters. Compared to an MD membrane, Langevin particles were more likely to be in a 14-particle cluster, the maximum cluster size, or exist as a single particle and 13-particle cluster. MD simulations showed increased sampling of mid-range cluster sizes.

To further explore the relative stability of clusters sampled in Langevin and MD simulations, we quantified the time evolution of cluster membership (**Figure 6**). Area charts of the number of particles in clusters of size 1-14 were mapped over time and smoothed with a 5-point moving average. Both Langevin and MD simulations exhibited intermittent changes in cluster size over the length of the simulation. This demonstrates that although Langevin dynamics simulations simplify thermal forces from other lipids and the surrounding solution into an implicit random force, these forces are still sufficient to cause receptor dissociation events. However, these results again suggest that clusters in Langevin dynamics simulations are more stable than MD clusters. Similar analysis of cluster size evolution with a 2 mol% GD1a composition membrane indicates decreased cluster stability (data not shown). Because the difference is not in a consistent direction, this suggests that the variation between Langevin and MD cluster size distributions is likely due to approximation of the receptor pair potential. Although it's important to note differences in cluster membership, the general cluster size distributions

do not show a statistically significant difference. We therefore conclude that our Langevin dynamics membrane model captures the size distribution of receptor clusters with sufficient accuracy within the given timescale. Further analysis would be necessary to evaluate agreement between Langevin and MD cluster size distributions at experimental-length timescales on the order of minutes.

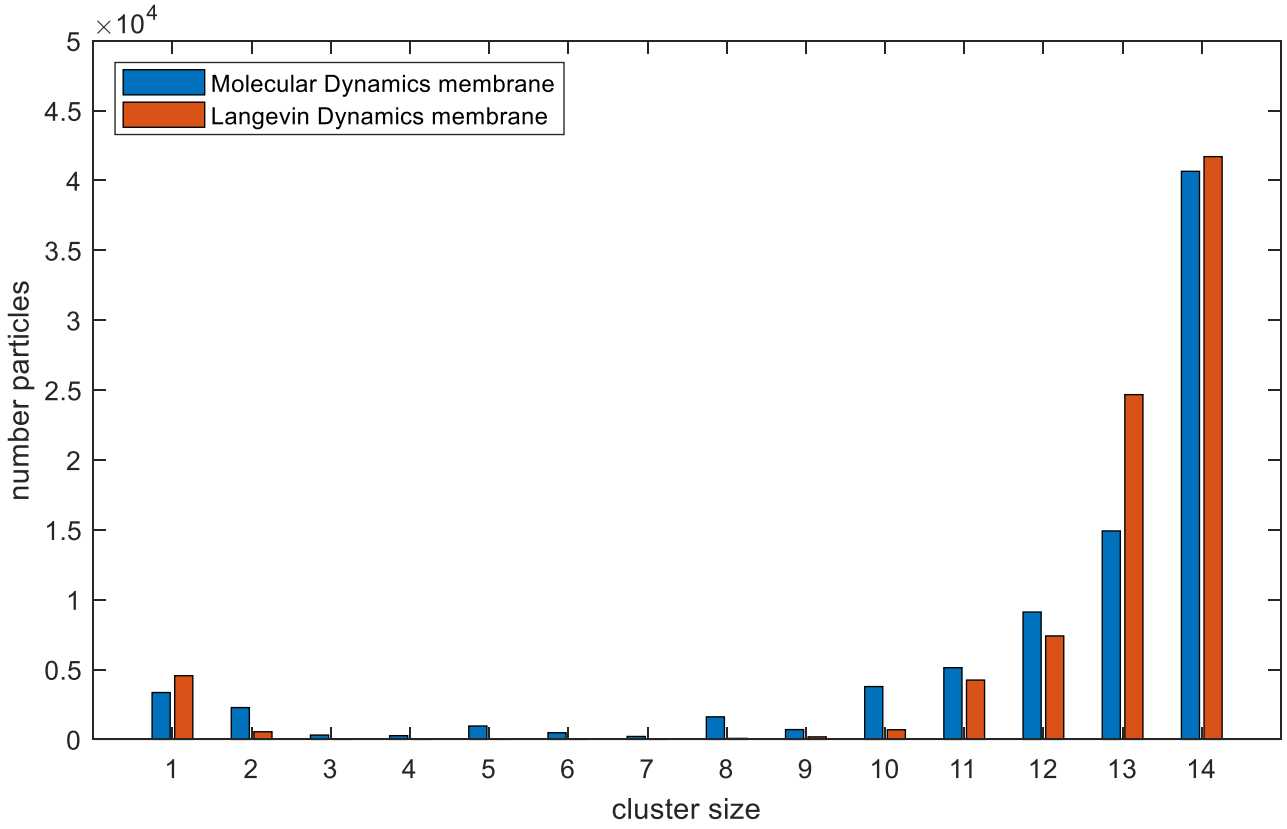

Figure 5. Comparison of Langevin and molecular dynamics simulated membrane cluster size distributions. Number of particles in clusters of size 1-14 accumulated over all simulation frames. In blue are clusters from a 4 mol% GD1a, 10 mol% cholesterol molecular dynamics membrane with means averaged across two leaflets. In orange are clusters from a 4 mol% GD1a, implicit 10 mol% cholesterol Langevin dynamics membrane with means averaged across three trials.

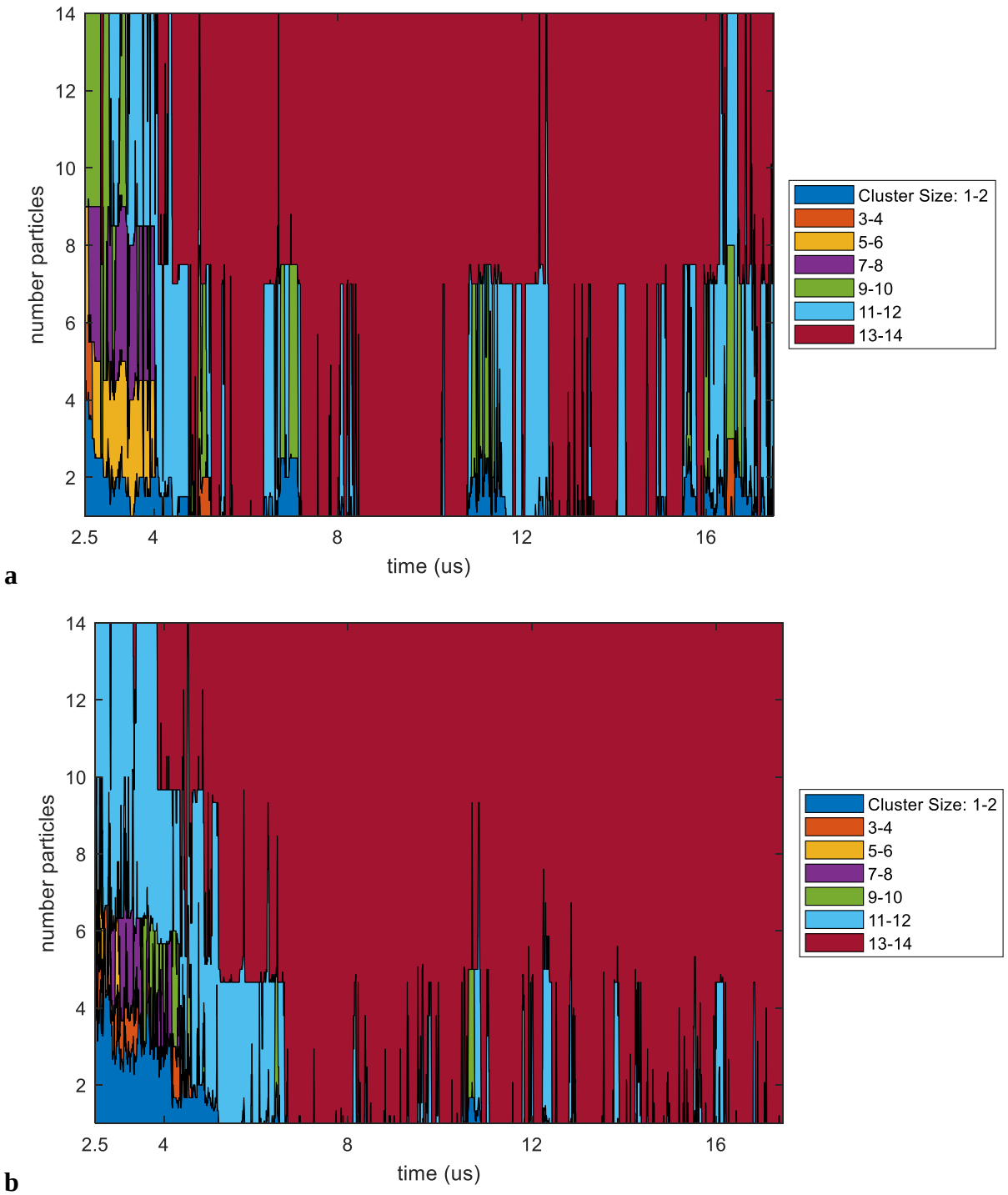

Figure 6. Comparison of Langevin and molecular dynamics simulated membrane cluster size evolution. (a) 4 mol% GD1a, 10 mol% cholesterol molecular dynamics membrane: number of particles in clusters of size 1-14 over the simulation time course. Numbers of particles for given cluster sizes are smoothed with a five-point moving average and averaged across two leaflets. **(b)** 4 mol% GD1a, implicit 10 mol% cholesterol Langevin dynamics membrane: number of particles in clusters of size 1-14 accumulated over the simulation time course. Numbers of particles for given cluster sizes are smoothed and averaged across three trials.

2.3.2 Validation of membrane receptor dissociation rate

In addition to cluster size distribution, we also evaluated the dissociation rate of a single GD1a receptor from clusters of any size. We chose to measure dissociation from all cluster sizes in order to increase sampling; this metric was expected to be unbiased because KS test statistical analysis revealed no statistically significant difference between Langevin and MD cluster size distributions.

Dissociation rates calculated from Langevin simulations did not consistently agree with the dissociation rate calculated from MD simulation. One of three Langevin dynamics trials predicted a dissociation rate in high agreement with the MD two-leaflet average. This trial had the most narrow probability distribution of the three, suggesting increased certainty (**Figure 7a**). However, there was high variability in estimated dissociation rate across the three Langevin dynamics trials. If the dissociation rate probability distributions for the three Langevin dynamics trials are averaged, two peaks emerge. The primary peak agrees well with MD simulation results, but a secondary peak suggests a larger dissociation rate (**Figure 7b**). A larger dissociation rate was not expected as previous cluster size distribution analysis demonstrated increased stability of Langevin dynamics clusters compared to MD membrane clusters.

Across all three trials, dissociation rate analysis of Langevin dynamics simulations results in significantly less sampling of dissociation events than analysis of MD simulations. This decreased frequency causes the increased variability in the predicted dissociation rate between Langevin trials. In fact, as sampling is doubled from 0.02 μs intervals to 0.01 μs intervals in the Langevin dynamics analysis, the probability distributions narrow and shift leftward toward the MD predicted dissociation rate (**Figure 8**). This suggests that the underlying receptor physics of Langevin simulations is reflective of MD membrane behavior. Differences in sampling may be a result of variation in cluster evolution captured by previous cluster size distribution analyses, or may be an artifact arising from different cutoff criteria in the analysis procedures for the two membrane models. The Langevin and MD membranes may feature events that vary from the given dissociation event definition, but that equally embody receptor dissociation behavior. The different cutoff criteria for the two membrane models may differently capture these dissociation event variations.

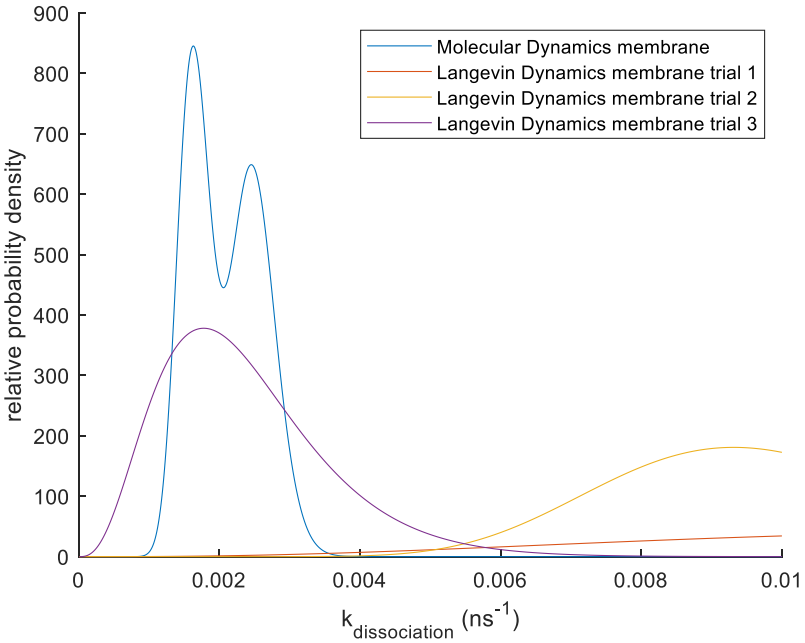

a

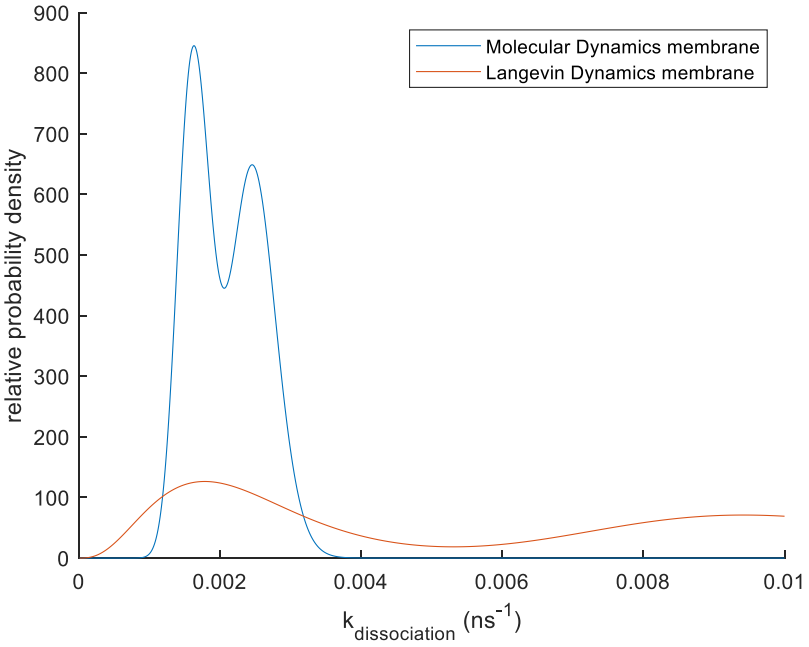

b

Figure 7. Comparison of Langevin and molecular dynamics simulated membrane receptor dissociation rates. (a) Probability density functions (PDFs) estimating the receptor dissociation rate constant. PDFs are shown for the two-leaflet average of a 4 mol% GD1a, 10 mol% cholesterol molecular dynamics membrane as well as for multiple Langevin dynamics trials of comparable membrane composition. **(b)** PDFs estimating the receptor dissociation constant averaged across both molecular dynamics leaflets and three Langevin dynamics trials.

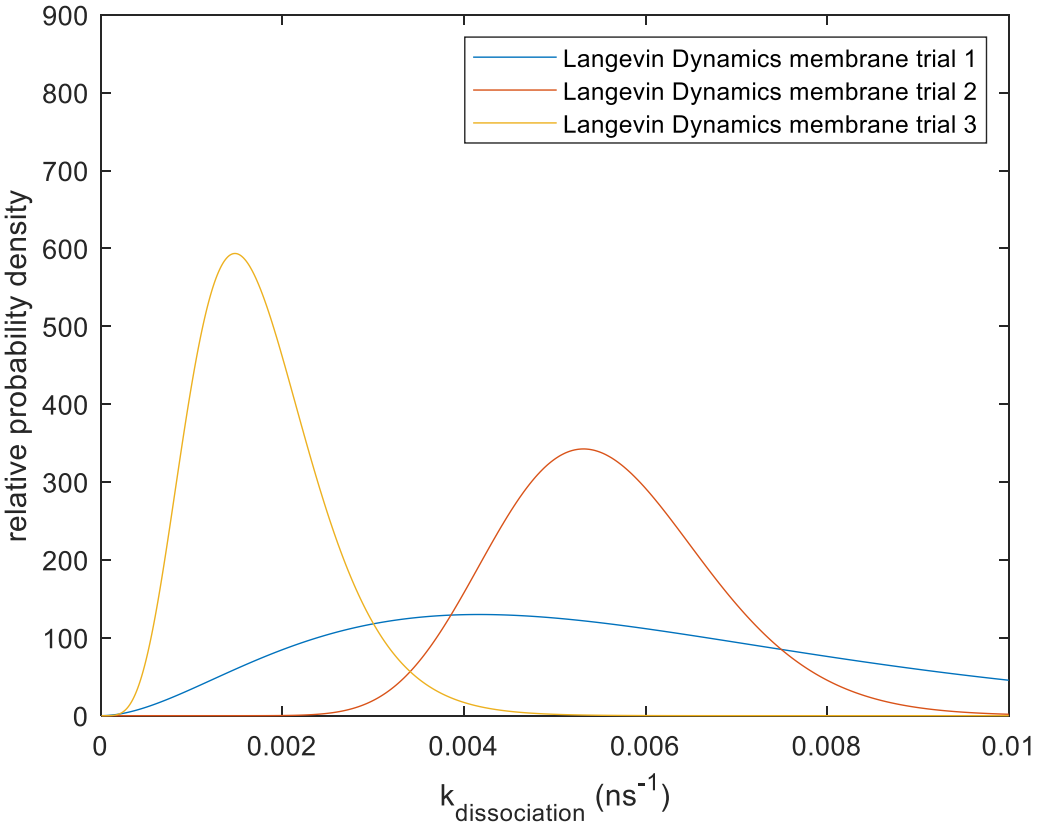

Figure 8. Receptor dissociation rate estimated by Langevin dynamics membranes decreases with increased sampling. Probability density functions (PDFs) estimating the receptor dissociation rate constant. PDFs are shown for three 4 mol% GD1a, implicit 10 mol% cholesterol Langevin dynamics membranes with increased sampling.

Chapter 3. Viral Binding

3.1 Chapter Introduction

We aimed to develop a model to mechanistically study the effect of membrane composition-driven receptor patterning on influenza binding to a human cell membrane. Here we evaluate how well our simulated viral outcomes recapitulate those resulting from experimental changes in membrane composition. We analyze membranes across a range of GD1a and cholesterol compositions in order to accurately capture the complex relationship between membrane composition and receptor patterning and dynamics. The strengths of our approach suggest insights on multivalent viral binding to an inhomogeneous host membrane, and the limitations highlight the bounds on our current assumptions and theory of influenza attachment.

3.2 Methods

Viral binding simulations were run with membrane GD1a compositions of 0.25, 2, 4, and 10 mol%. This amounted to 728, 5103, 10206, and 26244 particles, respectively, in a square membrane of 419.4 nm edge length. Receptor-receptor tabulated pair-potentials derived from membranes of 0, 10, and 20 mol% cholesterol were used to implicitly vary cholesterol composition. 0.25 mol% GD1a simulations were run with only 10 mol% cholesterol, and 2 mol% GD1a simulations with only 0 and 10 mol% cholesterol in parallel with observed experimental differences in receptor dissociation rate (23). Control simulations were run with a Lennard-Jones receptor pair potential.

A random initial pattern of receptors and unique seed for the HOOMD random force random number generator were assigned at the beginning of each simulation. The HOOMD Langevin dynamics function generated random numbers by hashing together the particle number, user seed, and current time step (43). The magnitudes of initial receptor velocities were set according to a Maxwell-Boltzmann distribution, and angles randomly defined in the xy-plane. A HOOMD tree neighbor list was used to efficiently evaluate inter-receptor forces (44). Membranes were equilibrated for 3 μs and then coupled to the mesoscopic viral binding and dynamics module for another 6 us. Receptor positions, virus center of mass and HA positions, HA-receptor bond events and lifetimes, and bond forces were recorded at 0.5 ns intervals over the simulation time course.

3.3Results

3.3.1 Comparing simulated and experimental viral binding outcomes and dependence on receptor concentration

We first evaluated the ability of our simulations to capture experimentally observed effects of varied membrane composition and local spatial patterning on influenza viral binding. Predicted binding outcomes were compared to microfluidic experiments in which the number of fluorescently labeled virions stably bound to a supported lipid bilayer was counted after 2.5 minutes of exposure (23). Although our us-length, single-virus binding simulations produced different measurable outputs than multi-virus, minute-length experimental binding assays, we assumed trends would be consistent across timescales. We classified stable viral binding in our simulations according to three criteria: a change in the mean number of bound receptors between time steps less than the increase in bound receptors at the initial time step of attachment, attachment to the membrane for at least 20% of the simulation time, and active attachment at the end of the simulation (29). Based on experimental data, we expected to observe a dependence on receptor concentration for stable viral binding. No stable binding was thus expected for membrane GD1a concentrations less than or equal to 0.25 mol%, stable binding was expected for GD1a concentrations greater than or equal to 1 mol%, and approximately all virions were expected to be stably attached to the membrane for GD1a concentrations equal to 10 mol%. These trends were expected over all cholesterol composition of 0-20 mol%.

According to the three criteria for stable binding, we observed that no virus was stably bound after 6 μs of simulation time across all membrane compositions (**Figure 9**). An increased number of bond formation events and an increased number bound receptors were observed with greater mol% GD1a, but intermittent no-bond periods were observed across all GD1a compositions as bonds were quickly broken due to viral movement. These results suggest that either our model underestimates viral binding, or that our definition of stable binding should be revised.

Throughout the simulation time, virus vertical position fluctuated within the 133 nm height expected from optical tweezers force spectroscopy experiments (**Figure 10b**) (25). However, it should be noted that spontaneous membrane fluctuations are unlikely to stretch a bonded virus this far from the membrane without the presence of an outside pulling force. The virus is therefore expected to remain much closer than this 133 nm distance. With this qualification in mind, the constant near-membrane

viral position suggests consistent virus-receptor interaction within the simulation time window for most trials.

It may be that unbroken virus-receptor attachment is not needed, but that stable binding depends on sufficiently small no-bond intervals and a critical mean number of bound receptors. For instance, the mean number of bound receptors (median of 4 trials) increases as (0.0151, 0.1044, 0.2266, 1.0350) with GD1a composition from 0.25 to 10 mol% (**Figure 11a**). The proportion time the virus is bound to the membrane (median of 4 trials) also increases as (0.0151, 0.0938, 0.1904, 0.5176) with GD1a composition (**Figure 11b**). These results suggest that viral binding depends on receptor concentration. However, experimental results specify that binding should saturate at a membrane GD1a composition of 4 mol% (23). A Kruskal-Wallis test followed by a Tukey's honest significant difference multiple comparison test also indicates a statistically significant difference in mean number bound receptors and proportion of time bound only between the 0.25 and 10 mol% GD1A compositions ($\alpha = 0.05$). Together, these results indicate that our model underestimates viral binding, displaying a decreased sensitivity to receptor concentration. Instead of observing stable, multivalent binding at membrane compositions of $\geq$1 mol% GD1a, we don't near a mean number of bound receptors when bound of at least two until GD1a concentration is increased to 10 mol% (**Figure 11c**).

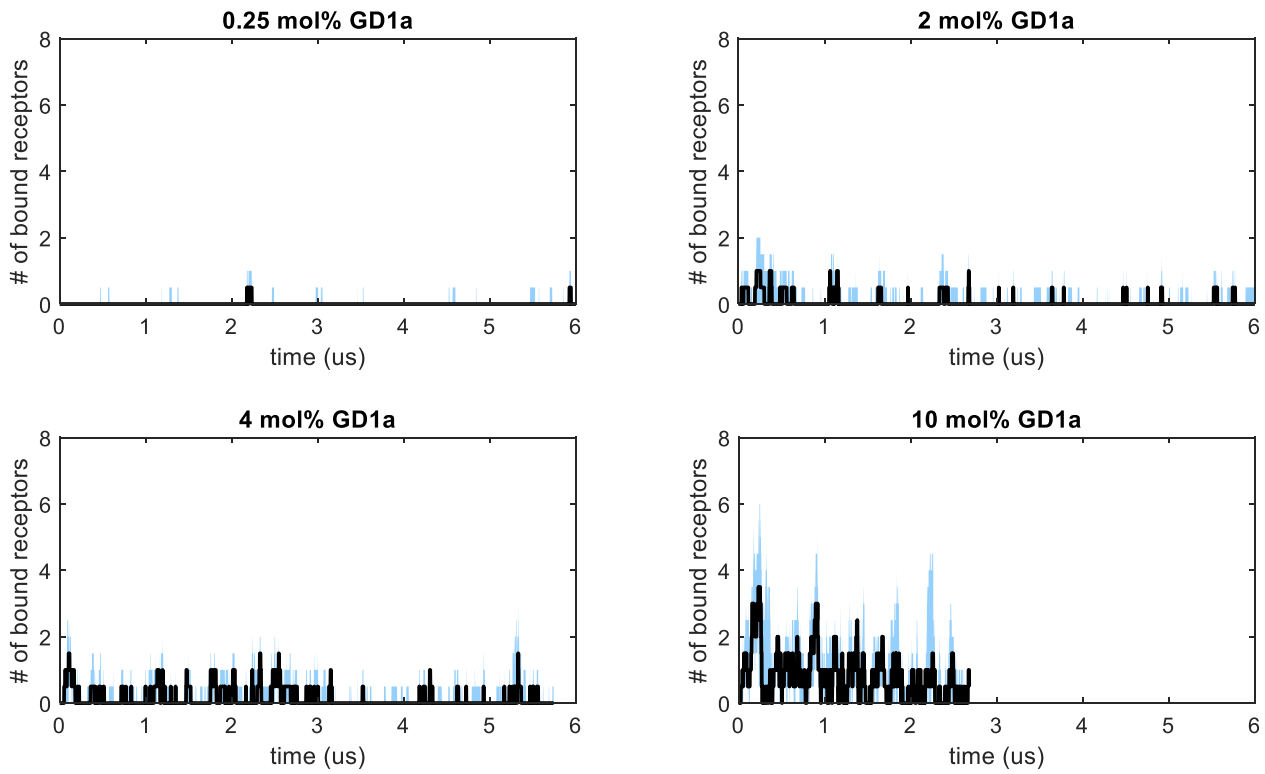

Figure 9. Intermittent periods of unbinding occur across membrane receptor compositions. Viral binding to simulated membranes of 0.25-10 mol% GD1a and 10 mol% cholesterol. Black represents the median number of bound receptors over time across 4 trials, and blue represents the interquartile range.

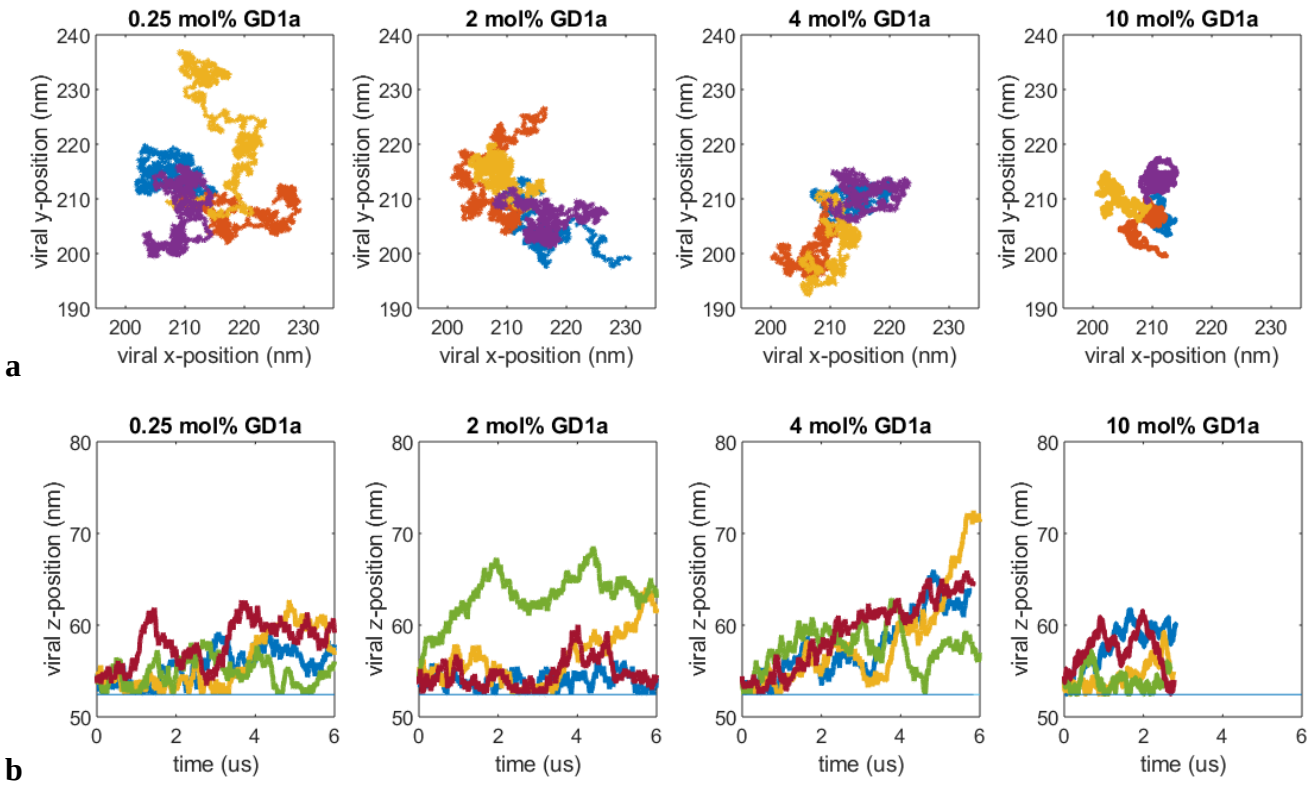

Figure 10. Virus movement relative to simulated membrane. (a) Virus center of mass movement in the xy-membrane plane. Different colored traces represent different trials. **(b)** Virus center of mass movement along the vertical z-axis. All traces remain below the 133 nm vertical cutoff for bond breakage. At a height of 52.4310 nm (blue line) the viral surface is touching the membrane.

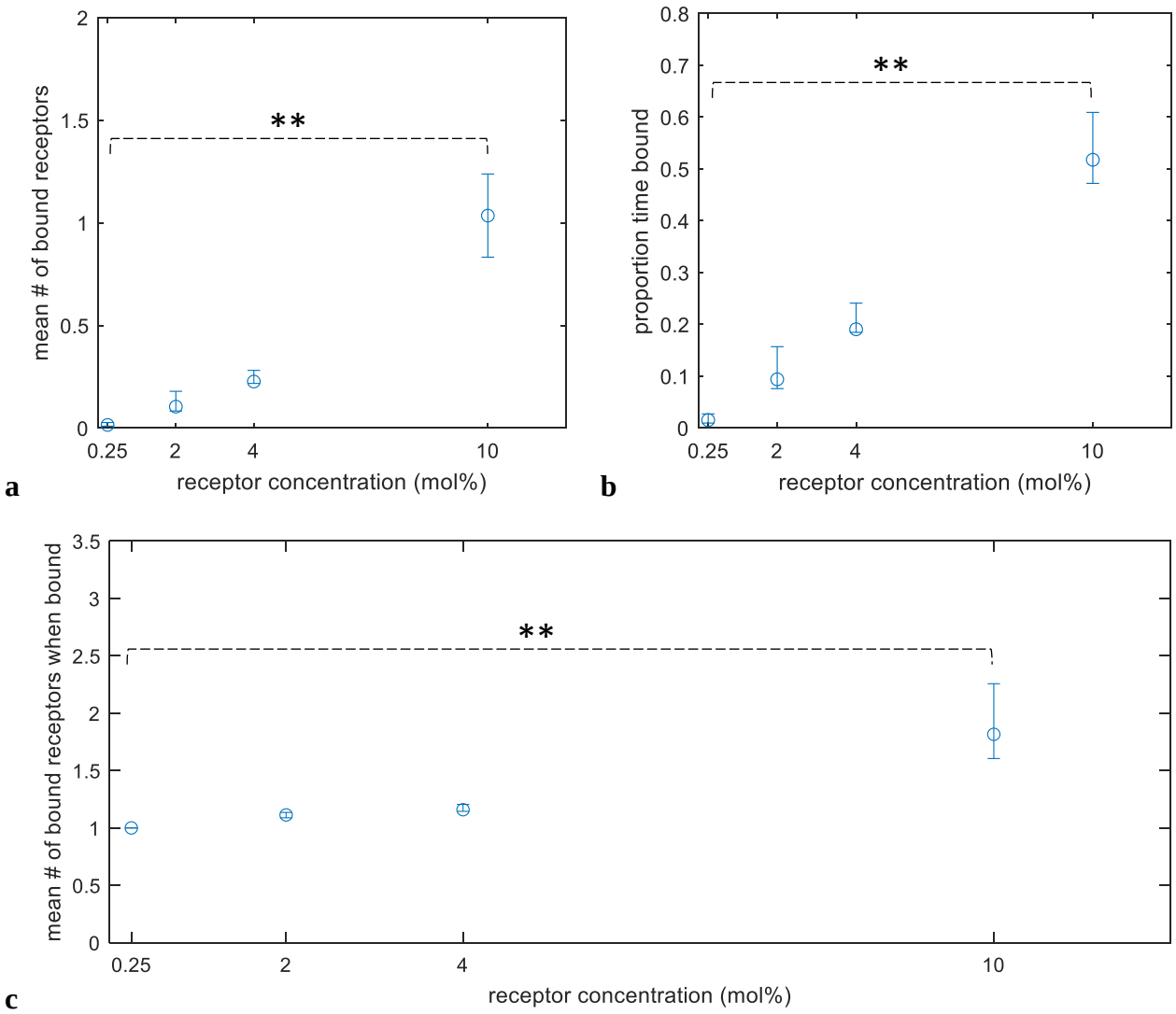

Figure 11. Viral binding to simulated membrane increases with GD1a composition to a lesser degree than experiment. (a) Mean number of bound receptors with increased membrane GD1a concentration. **(b)** Proportion of simulation time the virus spends bound to the membrane with increased GD1a concentration. **(c)** Mean number of bound receptors for timepoints when the virus is bound to the membrane with increased GD1a concentration. All means are averaged over the entire simulation time. Data points represent the median of 4 trials and error bars represent the interquartile range. **A pair-wise statistically significant difference was found between a 0.25 mol% GD1a, tabulated pair potential membrane and a 10 mol% GD1a, tabulated pair potential membrane.

3.3.2 Evaluating model sensitivity to localized receptor patterning

We then compared our simulated viral binding outcomes against control simulations parameterized with a Lennard-Jones (LJ) GD1a pair potential and across a range of cholesterol compositions. Simulations that included a tabulated GD1a pair potential with a deep attractive well featured a slightly increased mean number of bound receptors, proportion of time bound, and mean number of bound receptors when bound compared to simulations with the control LJ pair potential (**Figure 12a-c**). However, a Kruskal-Wallis test followed by a Tukey's honest significant difference multiple comparison test did not indicate a statistically significant difference in any of these three metrics for simulations with the same receptor concentration ($\alpha = 0.05$). A significant difference in the mean number of bound receptors or the proportion of time bound was only found between either 0.25 mol% GD1a simulation and 10 mol% GD1a simulations with a tabulated pair potential. A significant difference in the mean number of bound receptors when bound was only found between either 0.25 mol% GD1a simulation and either 10 mol% GD1a simulation. This non-definitive result suggests our model is only marginally sensitive to localized receptor patterning for the given sampling. Histograms of the number of GD1a receptors bound to the hemagglutinin on an influenza virus accumulated over the simulation time course reveal only one or two simultaneous influenza-membrane interactions with either pair potential (**Figure 13**). Although the specific receptors and hemagglutinin proteins interacting change throughout the simulation, only one or two of 150 HA available on the lower influenza hemisphere remain actively bound at a time.

Given decreased model sensitivity to receptor concentration, we are not powered to detect even finer cholesterol-dependent differences in viral binding (**Figure 14**). Although increased cholesterol composition was expected to increase the mean number of bound receptors and proportion of time bound, a Kruskal-Wallis test followed by a Tukey's honest significant difference multiple comparison test did not indicate a statistically significant difference in either of these metrics across simulation compositions ($\alpha = 0.05$). It is probable that our model could not detect the small changes in membrane characteristics invoked by a group of tabulated receptor pair potentials even more similar than the control Lennard Jones pair potential. Our 2 nm lateral breakage criterion may also cause bond breakage on a shorter time scale than differences in receptor dissociation rate previously observed with increased cholesterol composition (23). Therefore, although use of a membrane pair potential capturing GD1a-GD1a interaction marginally improves accuracy of trends in influenza binding, our model is even less sensitive to variations in cholesterol-dependent receptor patterning.

The literature demonstrates that membrane composition influences viral binding by altering localized receptor patterning and dynamics (23). We have hypothesized that cluster size and receptor dissociation rate are two metrics to capture membrane characteristics. Therefore, we analyzed the distribution of cluster sizes present in equilibrated membranes at the start of viral binding simulations (**Figures 15-18**). A two-sample, two-sided Kolmogorov-Smirnov (KS) test found no statistically significant difference between distributions of particles in clusters of size 1-4 in 0.25 mol% GD1a membranes with LJ and tabulated pair potentials ($\alpha = 0.05$) (**Figure 15b**). A significant difference was found between distributions of particles in clusters of size 1-15 for a 2 mol% GD1a membrane with a LJ pair potential and a 2 mol% GD1a, 10 mol% cholesterol membrane with a tabulated pair potential ($\alpha = 0.05$) (**Figure 16b**). No significant difference was seen between cluster size distributions for a 2 mol% GD1a membrane with a LJ pair potential and a 2 mol% GD1a, 0 mol% cholesterol membrane with a tabulated pair potential. A similar trend was seen for membranes with 4 mol% GD1a: a pairwise significant difference from a membrane parameterized with a LJ pair potential was only seen for membrane cholesterol compositions of at least 10 mol% (**Figure 17b**). At 10 mol% GD1a, a significant difference was observed between membranes with LJ and tabulated pair potentials across all cholesterol compositions (**Figure 18b**). Therefore, incorporating GD1a-GD1a interaction through a tabulated pair potential only consistently affects the cluster size distribution at a receptor concentration of 10 mol% GD1a. Increased cholesterol composition was expected to increase cluster stability and thus shift the cluster size distribution towards larger cluster sizes. A significant difference across cholesterol compositions was only observed between 0 and 10 mol% cholesterol for membranes with 10 mol% GD1a. These results suggest that our model lacks sensitivity to localized receptor patterning and dynamics because differences in these characteristics with the addition of GD1a-GD1a interaction or varied cholesterol composition are just very small.

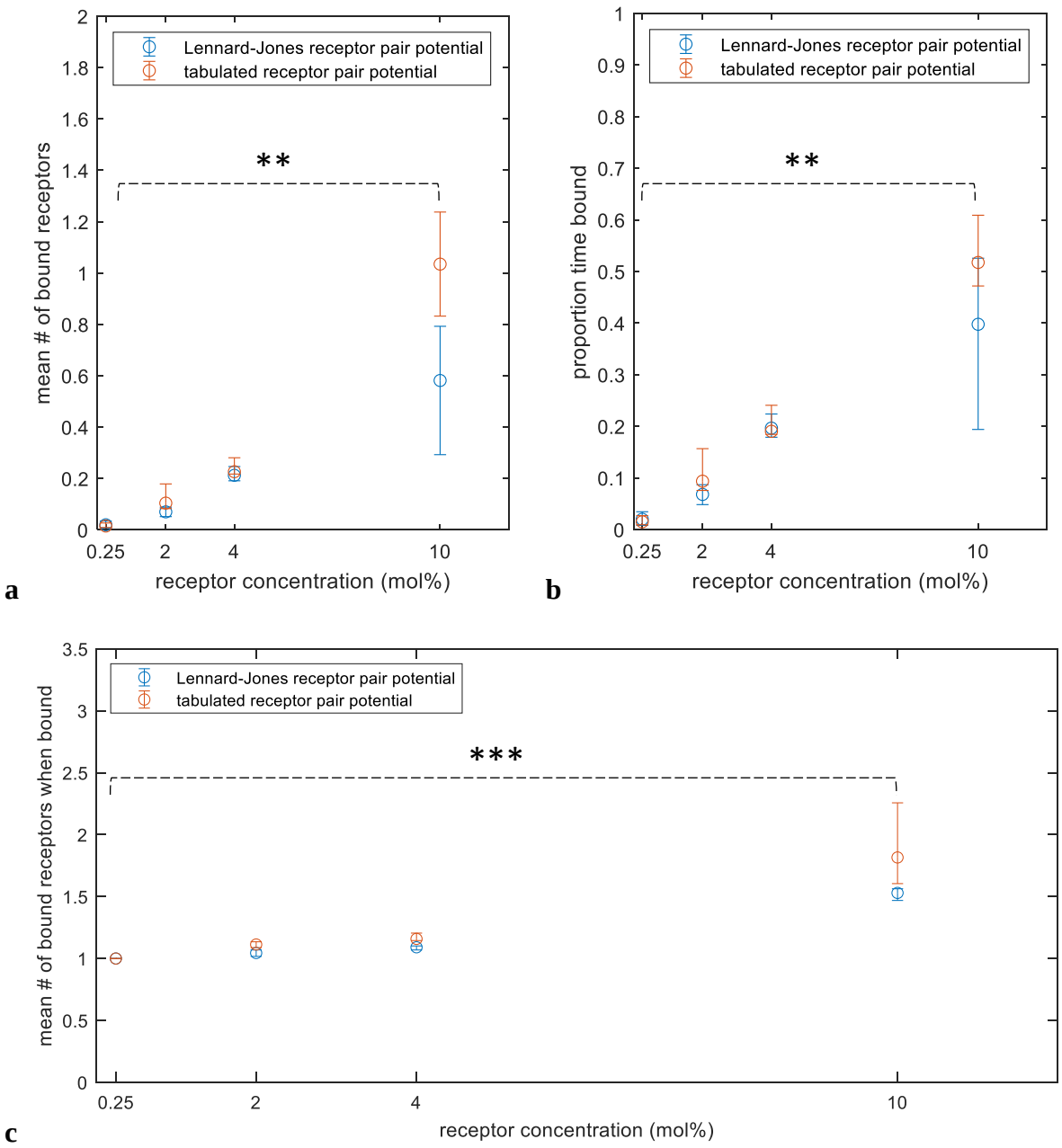

Figure 12. Simulation viral binding is somewhat sensitive to local membrane patterning. **(a)** Mean number of bound receptors with increased membrane GD1a concentration. **(b)** Proportion of simulation time the virus spends bound to the membrane with increased GD1a concentration. **(c)** Mean number of bound receptors for timepoints when the virus is bound to the membrane with increased GD1a concentration. All means are averaged over the entire simulation time. Data points represent the median of 4 trials and error bars represent the interquartile range. **A pair-wise statistically significant difference was found between a 0.25 mol% GD1a, tabulated pair potential membrane and a 10 mol% GD1a, tabulated pair potential membrane; and between a 0.25 mol% GD1a, LJ pair potential membrane and a 10 mol% GD1a, tabulated pair potential membrane. ***In addition to the above, a pair-wise statistically significant difference was also found between a 0.25 mol% GD1a, tabulated pair potential membrane and a 10 mol% GD1a, LJ pair potential membrane; and between a 0.25 mol% GD1a, LJ pair potential membrane and a 10 mol% GD1a, LJ pair potential membrane.

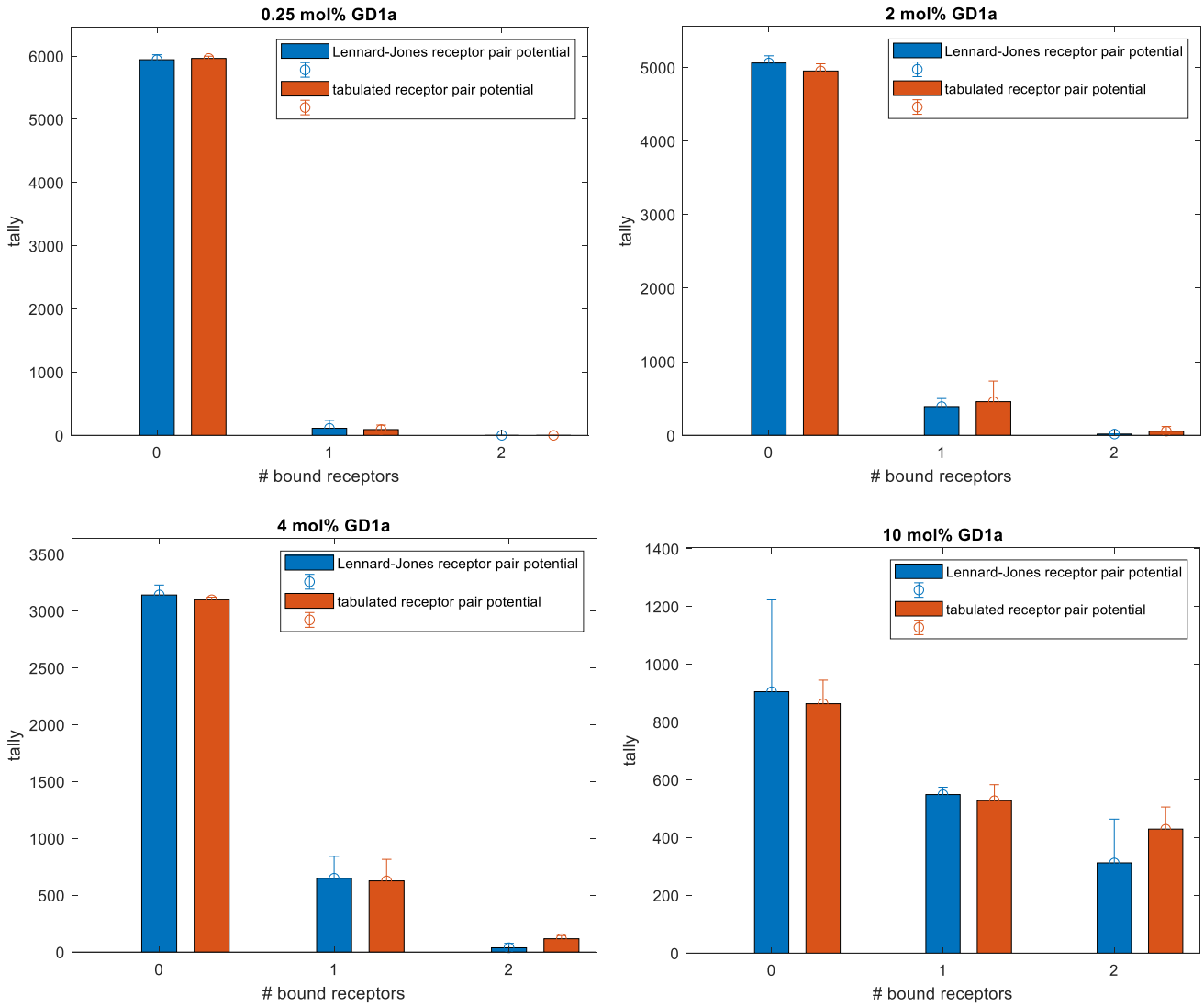

Figure 13. Number of GD1a receptors bound accumulated over the simulation time course. Histograms of the number of GD1a receptors bound to hemagglutinin on an influenza virus accumulated over the simulation time course. Bars represent the median of 4 trials and error bars represent the interquartile range.

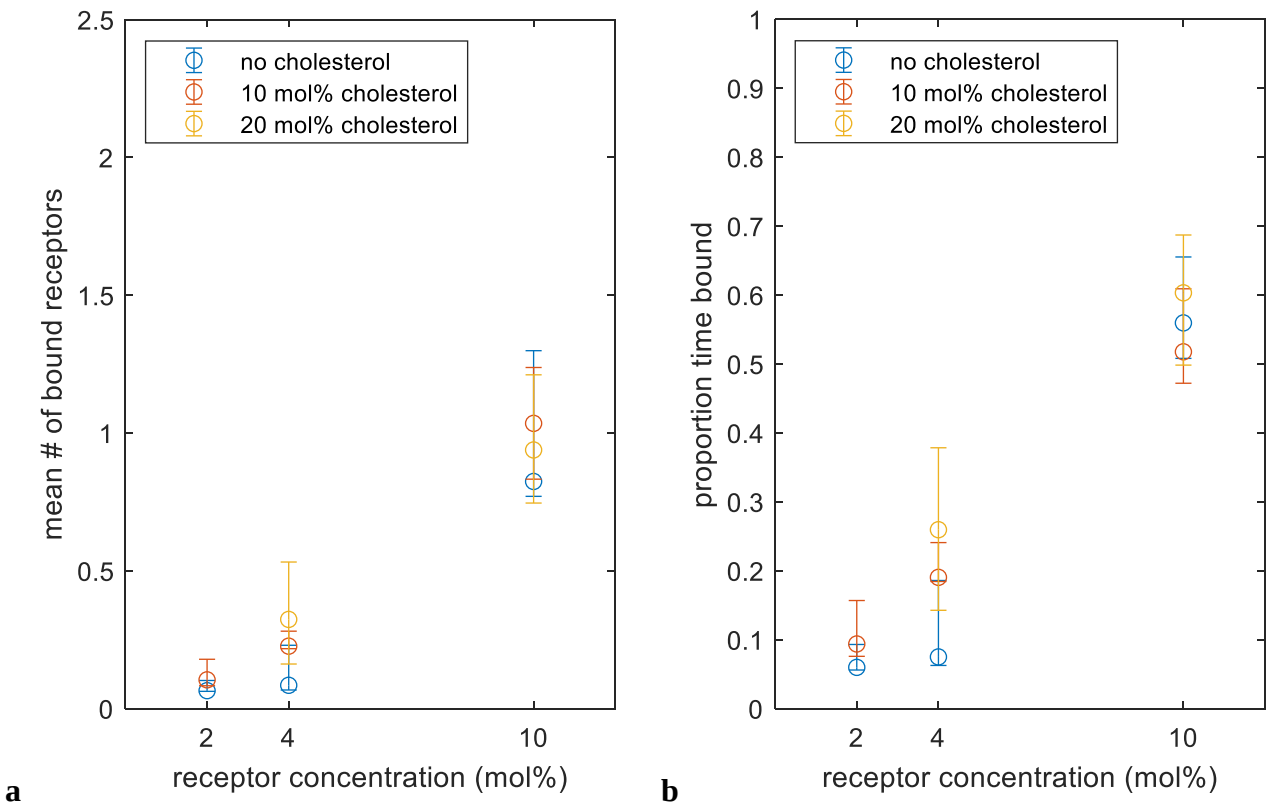

Figure 14. Simulation viral binding is insensitive to membrane cholesterol composition. **(a)** Mean number of bound receptors with increased membrane GD1a concentration. **(b)** Proportion of simulation time the virus spends bound to the membrane with increased GD1a concentration. All means are averaged over the entire simulation time. Data points represent the median of 4* trials and error bars represent the interquartile range. *Only 3 trials were used for analysis of membranes with 2 mol% GD1a, no cholesterol and 4 mol% GD1a, no cholesterol composition.

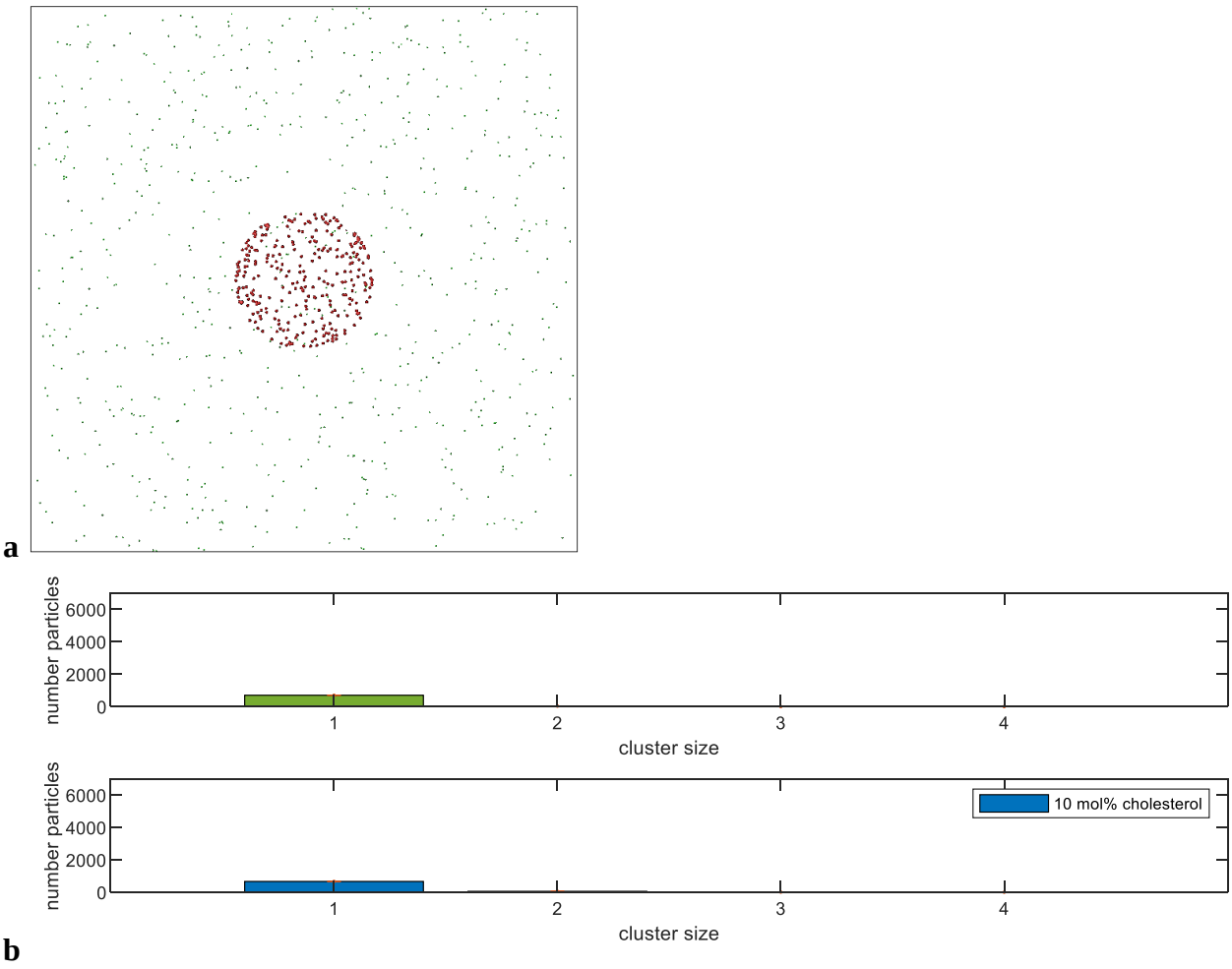

Figure 15. Comparison of cluster size distributions for 0.25 mol% membranes with and without GD1a-GD1a interaction. (a) Visualization of clustering in a simulated 0.25 mol% GD1a membrane with a tabulated pair potential. Receptors are green and viral HA projected onto the membrane plane are red. **(b)** Number of particles in clusters of size 1-4 accumulated over all simulation frames. Green represents membranes parameterized with a control Lennard Jones pair potential and blue represents membranes parameterized with a tabulated pair potential that captures GD1a-GD1a interaction. Bars represent the median of 4 trials and error bars represent the interquartile range.

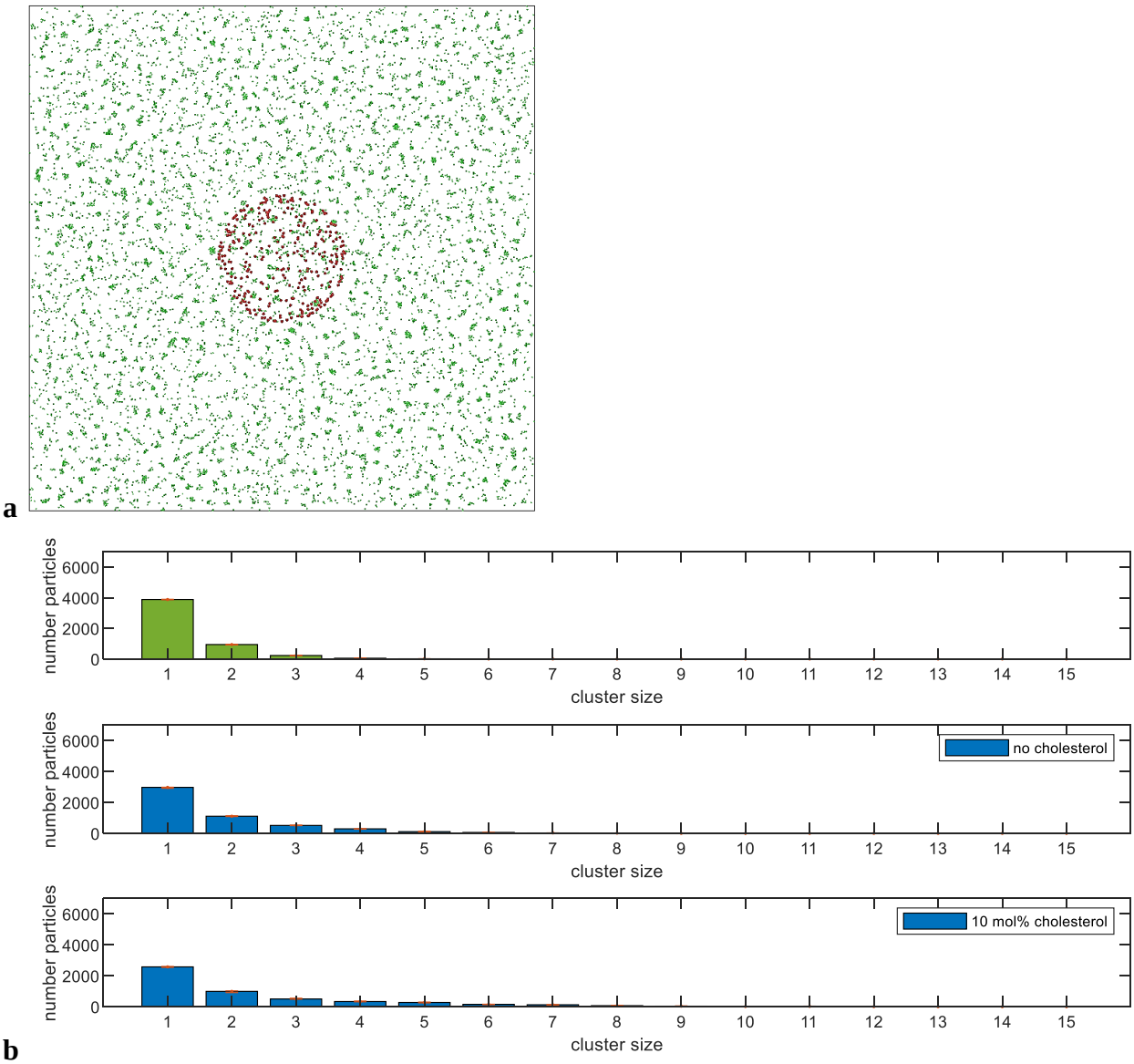

Figure 16. Comparison of cluster size distributions for 2 mol% membranes with and without GD1a-GD1a interaction and of varying cholesterol composition. (a) Visualization of clustering in a simulated 2 mol% GD1a membrane with a tabulated pair potential. Receptors are green and viral HA projected onto the membrane plane are red. **(b)** Number of particles in clusters of size 1-15 accumulated over all simulation frames. Green represents membranes parameterized with a control Lennard Jones pair potential and blue represents membranes parameterized with a tabulated pair potential that captures GD1a-GD1a interaction. Bars represent the median of 4* trials and error bars represent the interquartile range. *Only 3 trials were used for analysis of membranes with 2 mol% GD1a, no cholesterol composition.

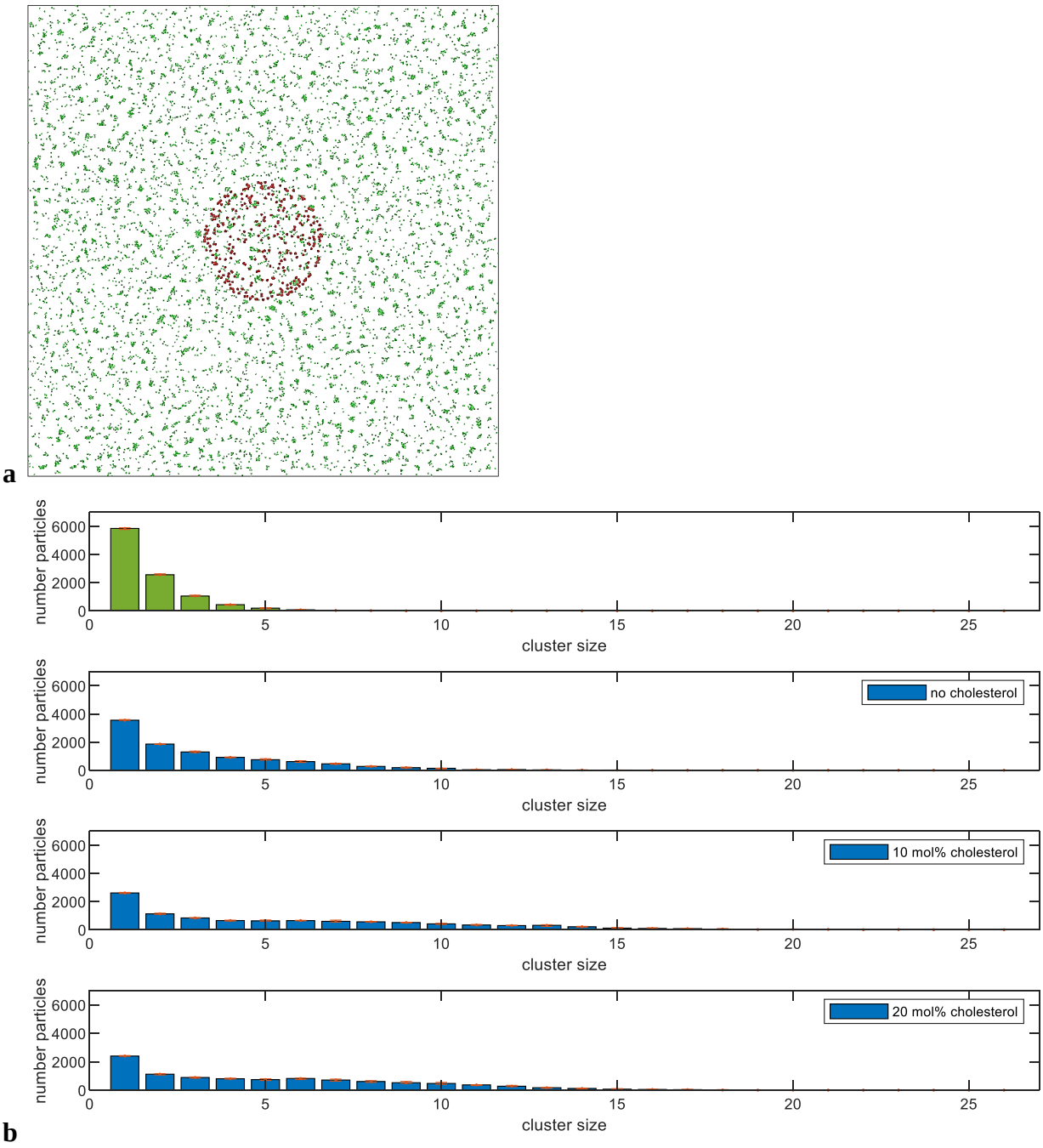

Figure 17. Comparison of cluster size distributions for 4 mol% membranes with and without GD1a-GD1a interaction and of varying cholesterol composition. (a) Visualization of clustering in a simulated 4 mol% GD1a membrane with a tabulated pair potential. Receptors are green and viral HA projected onto the membrane plane are red. **(b)** Number of particles in clusters of size 1-26 accumulated over all simulation frames. Green represents membranes parameterized with a control Lennard Jones pair potential and blue represents membranes parameterized with a tabulated pair potential that captures GD1a-GD1a interaction. Bars represent the median of 4* trials and error bars represent the interquartile range. *Only 3 trials were used for analysis of membranes with 4 mol% GD1a, no cholesterol composition.

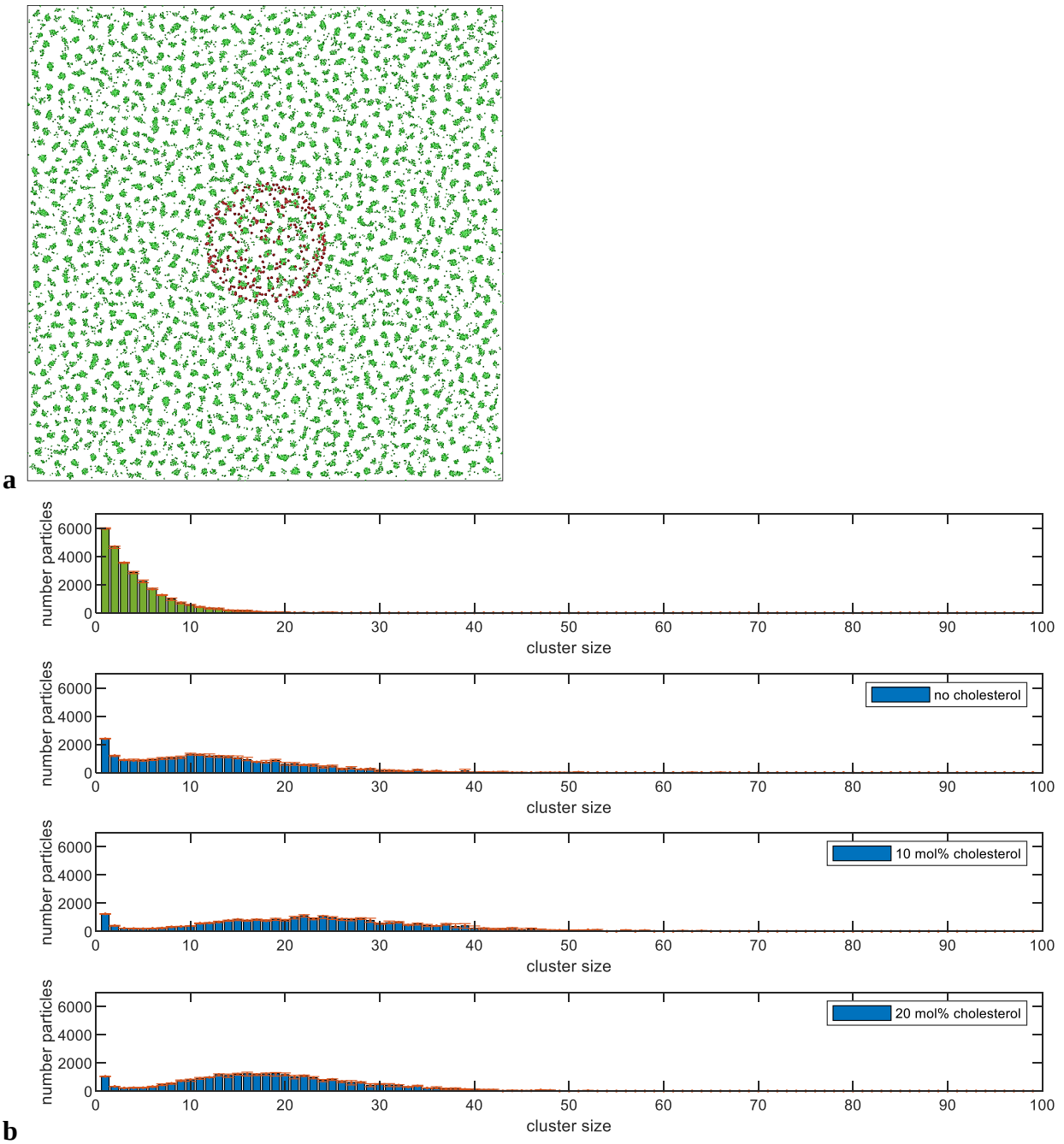

Figure 18. Comparison of cluster size distributions for 10 mol% membranes with and without GD1a-GD1a interaction and of varying cholesterol composition. (a) Visualization of clustering in a simulated 10 mol% GD1a membrane with a tabulated pair potential. Receptors are green and viral HA projected onto the membrane plane are red. **(b)** Number of particles in clusters of size 1-99* accumulated over all simulation frames. Green represents membranes parameterized with a control Lennard Jones pair potential and blue represents membranes parameterized with a tabulated pair potential that captures GD1a-GD1a interaction. Bars represent the median of 4 trials and error bars represent the interquartile range. *A single 99-particle cluster existed for one 10 mol% GD1a, 10 mol% cholesterol membrane trial. All other clusters contained 66 particles or fewer.

3.3.3 Evaluating membrane remodeling

In addition to evaluating membrane patterning as a determinant of influenza viral binding, we applied our model to interrogate the reverse: the impact of viral attachment on the membrane. It remains unknown whether the influenza virus can readily bind to an equilibrium distribution of receptors, or whether virus interaction with the membrane actively remodels this receptor distribution over time to improve binding favorability. However, with the 2 nm lateral cutoff for bond breakage in place, bond lifetimes were too short to distinguish receptor movement in response to viral binding forces. No significant difference was observed in the distribution of particles across cluster sizes accumulated over the simulation duration, with and without viral interaction (**Figure 19**). If large-scale receptor remodeling exists, such as a decrease in the lateral distance of all receptors to the viral center of mass, it occurs on a significantly longer time scale than that captured by our simulations.

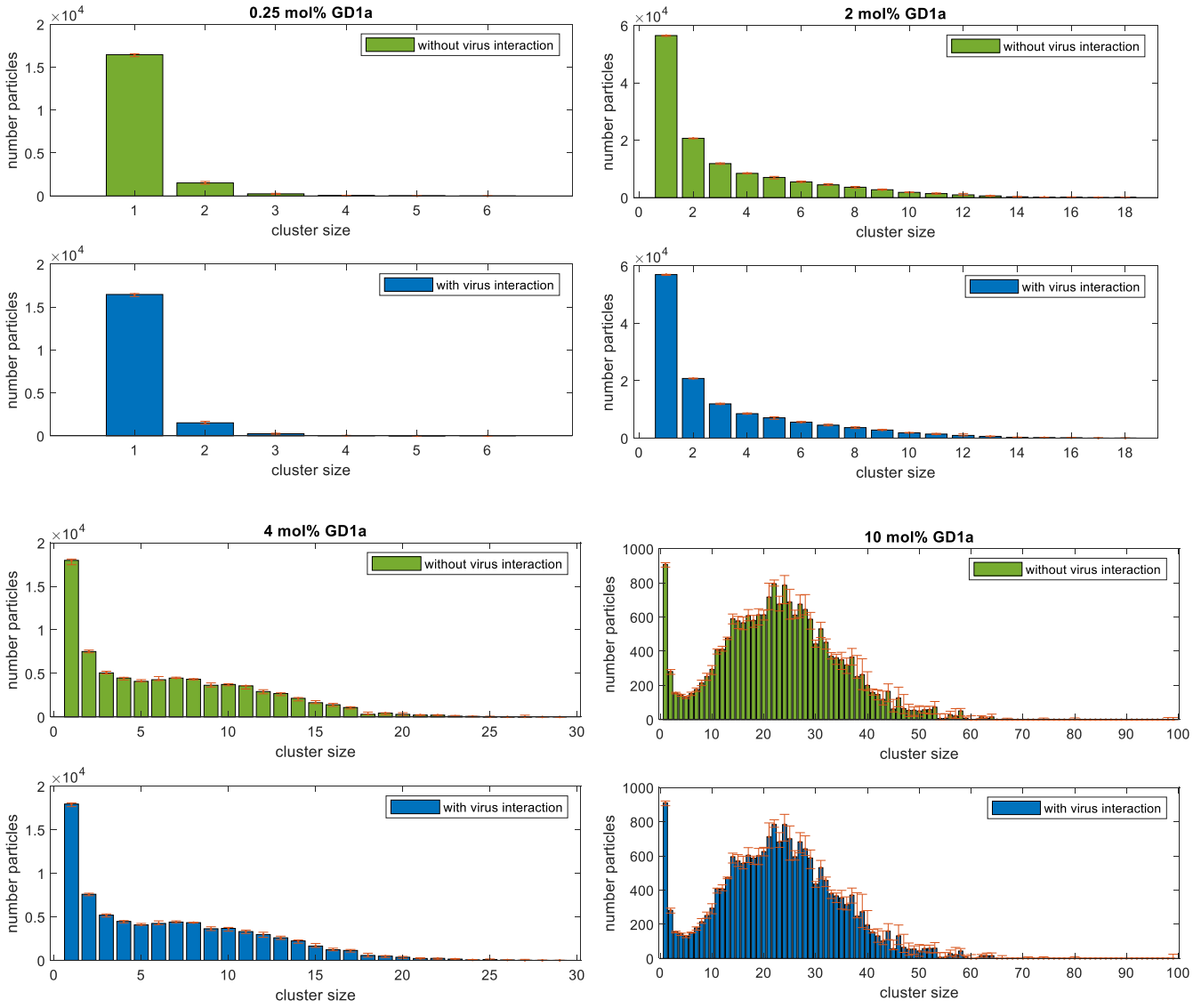

Figure 19. Membrane receptor remodeling by viral binding forces is not observed on a µs timescale. Number of particles across cluster sizes accumulated over the simulation duration at 60 ns intervals. Bars represent the median of 4 trials and error bars represent the interquartile range.

Chapter 4. Thesis Discussion and Future Directions

In this work, we developed a model that connects inhomogeneous influenza receptor patterning and dynamics information from molecular dynamics simulations to mesoscopic viral binding behavior. Validation analyses suggest that our Langevin dynamics membrane model displays a cluster size distribution reflective of higher-resolution MD simulations. Our membrane model likely exhibits a receptor dissociation rate comparable or greater than MD simulations. However, further refinement of our validation analysis methods is needed to evaluate agreement between Langevin and MD cluster size distributions and receptor dissociation rates at experimental-length timescales on the order of minutes.

For the same spatial scale, we achieved a reduction in run-time from weeks to days compared to MD simulations. Our model is also scalable to a virus-length spatial scale. However, at a virus-length spatial scale, our model is limited to sub-experimental time scales. The simulations used in this investigation were on the order of μs. For direct comparison of modeled binding outcomes to experimental data, minutes of simulation time are needed. Our modeling approach allows us to collect real-time data on virus-membrane interaction, complementing *in vitro* experiments that output binary snapshots of binding or no binding. This information has the potential to add mechanistic detail to the physical theory of multivalent virus-membrane interaction.

However, failure of our model to recapitulate expected viral binding outcomes highlights the limitations of our current approach. Although metrics such as mean number of bound receptors and proportion time bound tended to increase with receptor concentration, a statistically significant effect was only observed when GD1a composition was increased from 0.25 to 10 mol%. Viruses also only bound multivalently, or to more than a single receptor on average, for 10 mol% membrane GD1a compositions. Similarly, our simulations revealed a small but statistically insignificant response to GD1a self-interaction. In conjunction with lack of sensitivity of viral binding outcomes to varied cholesterol composition, these results suggest our model is not sufficiently powered to detect differences in localized receptor spatial patterning and dynamics. With our current model parameterization, we also did not observe large-scale membrane remodeling to improve binding favorability. However, lack of agreement between simulated and experimental observations of influenza binding behavior provide an opportunity for us to reexamine some of our fundamental assumptions:

Simulation length

A fundamental difference between simulations and experiments was time scale. While experiments measured binding outcomes after 2.5 minutes, limitations to model run time efficiency only allowed μs of simulation time. If modifications to the model enabled an increased time step, it would be interesting to run simulations for a full 2.5 minutes. The current model parameterization suggests that individual GD1a-HA bonds are constantly changing even during multivalent viral binding. Increased simulation time would allow us to further explore this hypothesis as well as the relevance of the intermittent unbinding events we observed across membrane compositions.

Impact of flow on viral binding

Experimental binding outcomes were derived from microfluidic experiments in which the number of fluorescently labeled virions stably bound to a supported lipid bilayer was counted after 2.5 minutes of exposure. The flow rate in these experiments was 50 uL/min. It was assumed that this flow rate could be neglected. However, the flow rate does lead to replacement of the simulation volume multiple times throughout the simulation time course. In recent experiments, the presence of flow has been qualitatively described to drastically increase the number of viral binding and fusion events compared to a longer exposure time with no flow. Addition of flow in a future model iteration therefore has the potential to increase viral binding outcomes.

Membrane deformability and the phenomenological model of bond formation and breakage

Experimental optical tweezers force spectroscopy measurements of the vertical spring constant of a single GD1a-HA harmonic bond were conducted with cells and therefore include membrane deformability (25). Although using this value in our model increased agreement with physiology, it also added an additional degree of vertical bond flexibility compared to baseline viral binding experiments with a supported bilayer (23). We would expect increased vertical flexibility to increase rather than decrease viral binding, but this difference could have caused a yet unknown effect on simulation results.

Combination of membrane deformability, receptor headgroup and HA flexibility, and the actual receptor-HA molecular binding interaction into a single spring constant also reduces physical detail of modeled viral binding events. Combined with the two nm lateral cutoff for bond breakage, it is possible that the current algorithm for calculating probability of bond formation and breakage events does not have the molecular resolution to detect local differences in receptor spatial patterning and dynamics. The

model would thus be improved by explicitly dividing out these components as individual forces. This would particularly improve model resolution in the lateral direction and increase lateral interaction forces, increasing the potential for membrane remodeling or modulation of viral movement by membrane attachment. Separation of components would also better account for the vertical tolerance of adjacent receptors: vertical flexibility should not vary widely across a small membrane section. It is necessary to improve model handling of membrane deformation as local curvature influences the lateral partitioning of glycosphingolipids, as well as other lipids (45). The timescale of viral binding events would also be predicted more accurately as the membrane deformability component could be applied only after the virus became sufficiently close or established a critical number of membrane bonds. However, additional experiments or simulations would be needed to derive the values for these separate components.

Membrane composition-dependent receptor patterning and dynamics

In addition to reconsidering the above assumptions parameterized into the mesoscopic viral binding module, additional steps can be taken to improve our Langevin dynamics membrane module. The GD1a diffusion coefficient was approximated from fluorescence recovery after photobleaching (FRAP) bulk fluidity measurements of lipid-tailed dye in a planar bilayer of similar composition. Measurements of the mean squared displacement of GD1a in molecular dynamics simulations could be used to derive a diffusion value more specific to GD1a. The potential of mean force (PMF) is also only a first-order approximation of the GD1a pair potential. Thermodynamic Monte Carlo simulations can be used to iteratively refine this estimation (46,47). Refinement of the pair potential would be particularly beneficial for parameterizing membranes of varying cholesterol composition because the calculated PMFs are currently very similar.

It is clear that despite the limitations of our model, much can be learned by thinking through the strengths and weaknesses of our current setup. Because hemagglutinin is modeled as evenly distributed throughout the viral envelope, and there are plentiful receptors available at high membrane GD1a compositions, the current method for calculating bond formation and breakage is likely the limiting factor for multivalent viral binding. Additional refinement of our membrane model may also contribute increased sensitivity to localized receptor patterning and dynamics. The current model provides a well-defined framework to implement these future modifications and additions.

References

1. Estimating Seasonal Influenza-Associated Deaths in the United States | Seasonal Influenza (Flu) | CDC [Internet]. 2018 [cited 2018 Jun 9]. Available from: https://www.cdc.gov/flu/about/disease/us_flu-related_deaths.htm

2. McKimm-Breschkin JL. Resistance of influenza viruses to neuraminidase inhibitors — a review. Antiviral Res. 2000;47(1):1–17.

3. Hay AJ, Zambon MC, Wolstenholme AJ, Skehel JJ, Smith MH. Molecular basis of resistance of influenza A viruses to amantadine. J Antimicrob Chemother. 1986;18:19–29.

4. Belshe RB, Smith MH, Hall CB, Betts R, Hay AJ. Genetic basis of resistance to rimantadine emerging during treatment of influenza virus infection. J Virol. 1988;62(5):1508–12.

5. Pinto LH, Holsinger LJ, Lamb RA. Influenza virus M2 protein has ion channel activity. Cell. 1992;69(3):517–28.

6. Govorkova EA, McCullers JA. Therapeutics Against Influenza. Swine Influenza. 2011;370:273–300.

7. Malakhov MP, Aschenbrenner LM, Smee DF, Wandersee MK, Sidwell RW, Gubareva LV, et al. Sialidase Fusion Protein as a Novel Broad-Spectrum Inhibitor of Influenza Virus Infection. Antimicrob Agents Chemother. 2006;50(4):1470–9.

8. Skehel JJ, Wiley DC. Receptor Binding and Membrane Fusion in Virus Entry: The Influenza Hemagglutinin. Annu Rev Biochem. 2000;69:531–69.

9. Couceiro JNSS, Paulson JC, Baum LG. Influenza virus strains selectively recognize sialyloligosaccharides on human respiratory epithelium; the role of the host cell in selection of hemagglutinin receptor specificity. Virus Res. 1993;29(2):155–65.

10. Riel D van, Munster VJ, Wit E de, Rimmelzwaan GF, Fouchier RAM, Osterhaus ADME, et al. Human and Avian Influenza Viruses Target Different Cells in the Lower Respiratory Tract of Humans and Other Mammals. Am J Pathol. 2007;171(4):1215–23.

11. Shinya K, Ebina M, Yamada S, Ono M, Kasai N, Kawaoka Y. Avian flu: Influenza virus receptors in the human airway. Nature. 2006;440(7083):435.

12. Sauter NK, Bednarski MD, Wurzburg BA, Hanson JE, Whitesides GM, Skehel JJ, et al. Hemagglutinins from two influenza virus variants bind to sialic acid derivatives with millimolar dissociation constants: a 500-MHz proton nuclear magnetic resonance study. Biochemistry (Mosc). 1989;28(21):8388–96.

13. Gui L, Ebner JL, Mileant A, Williams JA, Lee KK. Visualization and Sequencing of Membrane Remodeling Leading to Influenza Virus Fusion. J Virol. 2016;90(15):6948–62.

14. Chlanda P, Mekhedov E, Waters H, Schwartz CL, Fischer ER, Ryham RJ, et al. The hemifusion structure induced by Influenza virus haemagglutinin is determined by physical properties of the target membranes. Nat Microbiol. 2016;1(6):16050.

15. Lee DW, Hsu H-L, Bacon KB, Daniel S. Image Restoration and Analysis of Influenza Virions Binding to Membrane Receptors Reveal Adhesion-Strengthening Kinetics. PLOS ONE. 2016;11(10):e0163437.

16. Lakadamyali M, Rust MJ, Zhuang X. Endocytosis of influenza viruses. Microbes Infect. 2004;6(10):929–36.

17. Almeida RFM, Loura LMS, Fedorov A, Prieto M. Lipid Rafts have Different Sizes Depending on Membrane Composition: A Time-resolved Fluorescence Resonance Energy Transfer Study. J Mol Biol. 2005;346(4):1109–20.

18. Veatch SL, Keller SL. Separation of Liquid Phases in Giant Vesicles of Ternary Mixtures of Phospholipids and Cholesterol. Biophys J. 2003;85(5):3074–83.

19. Gu R-X, Ingólfsson HI, Vries AH de, Marrink SJ, Tieleman DP. Ganglioside-Lipid and Ganglioside-Protein Interactions Revealed by Coarse-Grained and Atomistic Molecular Dynamics Simulations. J Phys Chem. 2016;121(15):3262–75.

20. Yuan C, Furlong J, Burgos P, Johnston LJ. The Size of Lipid Rafts: An Atomic Force Microscopy Study of Ganglioside GM1 Domains in Sphingomyelin/DOPC/Cholesterol Membranes. Biophys J. 2002;82(5):2526–35.

21. Wessels L, Elting MW, Scimeca D, Weninger K. Rapid Membrane Fusion of Individual Virus Particles with Supported Lipid Bilayers. Biophys J. 2007;93(2):526–38.

22. Dennis Alford, Ellens H, Bentz J. Fusion of influenza virus with sialic acid-bearing target membranes. Biochemistry (Mosc). 1994;33(8):1977–87.

23. Goronzy IN, Rawle RJ, Boxer SG, Kasson PM. Cholesterol enhances influenza binding avidity by controlling nanoscale receptor clustering. Chem Sci. 2018;9(8):2340–7.

24. Domanska MK, Dunning RA, Dryden KA, Zawada KE, Yeager M, Kasson PM. Hemagglutinin Spatial Distribution Shifts in Response to Cholesterol in the Influenza Viral Envelope. Biophys J. 2015 Nov 3;109(9):1917.

25. Sieben C, Kappel C, Zhu R, Wozniak A, Rankl C, Hinterdorfer P, et al. Influenza virus binds its host cell using multiple dynamic interactions. Proc Natl Acad Sci U S A. 2012;109(34):13626.

26. Xu H, Shaw DE. A Simple Model of Multivalent Adhesion and Its Application to Influenza Infection. Biophys J. 2016;110(1):218–33.

27. English TJ, Hammer DA. Brownian Adhesive Dynamics (BRAD) for Simulating the Receptor-Mediated Binding of Viruses. Biophys J. 2004;86(6):3359–72.

28. Trister AD, Hammer DA. Role of gp120 Trimerization on HIV Binding Elucidated with Brownian Adhesive Dynamics. Biophys J. 2008;95(1):40–53.

29. Szklarczyk OM, González-Segredo N, Kukura P, Oppenheim A, Choquet D, Sandoghdar V, et al. Receptor Concentration and Diffusivity Control Multivalent Binding of Sv40 to Membrane Bilayers. PLOS Comput Biol. 2013;9(11):e1003310.

30. English TJ, Hammer DA. The Effect of Cellular Receptor Diffusion on Receptor-Mediated Viral Binding Using Brownian Adhesive Dynamics (BRAD) Simulations. Biophys J. 2005;88(3):1666–75.

31. Hutchinson EC, Charles PD, Hester SS, Thomas B, Trudgian D, Martínez-Alonso M, et al. Conserved and host-specific features of influenza virion architecture. Nat Commun. 2014;5:4816.

32. Bandlow V, Liese S, Lauster D, Ludwig K, Netz RR, Herrmann A, et al. Spatial Screening of Hemagglutinin on Influenza A Virus Particles: Sialyl-LacNAc Displays on DNA and PEG Scaffolds Reveal the Requirements for Bivalency Enhanced Interactions with Weak Monovalent Binders. J Am Chem Soc. 2017;139(45):16389–97.

33. Dembo M, Torney DC, Saxman K, Hammer D. The Reaction-Limited Kinetics of Membrane-to-Surface Adhesion and Detachment. Proc R Soc Lond. 1988;234(1274):55–83.

34. Bell GI. Models for the specific adhesion of cells to cells. Science. 1978;200(4342):618–27.

35. Wilson IA, Skehel JJ, Wiley DC. Structure of the haemagglutinin membrane glycoprotein of influenza virus at 3 Å resolution. Nature. 1981;289(5796):366–73.

36. Wang S, Shan X, Patel U, Huang X, Lu J, Li J, et al. Label-free imaging, detection, and mass measurement of single viruses by surface plasmon resonance. Proc Natl Acad Sci. 2010;107(37):16028–32.

37. Suzuki Y, Matsunaga M, Nagao Y, Taki T, Hirabayashi Y, Matsumoto M. Ganglioside GM1b as an influenza virus receptor. Vaccine. 1985;3(3):201–3.

38. Anderson JA, Lorenz CD, Travesset A. General purpose molecular dynamics simulations fully implemented on graphics processing units. J Comput Phys. 2008;227(10):5342–59.

39. Glaser J, Nguyen TD, Anderson JA, Lui P, Spiga F, Millan JA, et al. Strong scaling of general-purpose molecular dynamics simulations on GPUs. Comput Phys Commun. 2015;192:97–107.

40. Carton I, Malinina L, Richter RP. Dynamic Modulation of the Glycosphingolipid Content in Supported Lipid Bilayers by Glycolipid Transfer Protein. Biophys J. 2010 Nov 3;99(9):2947.

41. Floyd DL, Ragains JR, Skehel JJ, Harrison SC, Oijen AM van. Single-particle kinetics of influenza virus membrane fusion. Proc Natl Acad Sci U S A. 2008 Oct 7;105(40):15382.

42. Kasson PM, Ensign DL, Pande VS. Combining molecular dynamics with Bayesian analysis to predict and evaluate ligand-binding mutations in influenza hemagglutinin. J Am Chem Soc. 2009;131(32):11338–40.

43. Phillips CL, Anderson JA, Glotzer SC. Pseudo-random number generation for Brownian Dynamics and Dissipative Particle Dynamics simulations on GPU devices. J Comput Phys. 2011;230(19):7191–201.

44. Howard MP, Anderson JA, Nikoubashman A, Glotzer SC, Panagiotopoulos AZ. Efficient neighbor list calculation for molecular simulation of colloidal systems using graphics processing units. Comput Phys Commun. 2016;203:45–52.

45. Sorre B, Callan-Jones A, Manneville J-B, Nassoy P, Joanny J-F, Prost J, et al. Curvature-driven lipid sorting needs proximity to a demixing point and is aided by proteins. Proc Natl Acad Sci. 2009;106(14):5622–6.

46. Lyubartsev AP, Laaksonen A. Calculation of effective interaction potentials from radial distribution functions: A reverse Monte Carlo approach. Phys Rev E. 1995;52:3730.

47. Almarza NG, Lomba E. Determination of the interaction potential from the pair distribution function: An inverse Monte Carlo technique. Phys Rev E. 2003;68(1):011202.